

ISS 用 CO₂ 吸脱着装置の CO₂ 吸着特性に与える水分の影響

○吉田拓, 鈴木進補 (早大), 桜井誠人, 大西充 (JAXA)

Effect of Moisture Concentration on CO₂ Adsorption Characteristics of CO₂ Adsorption/Desorption Device for ISS

○Taku YOSHIDA, Shinsuke SUZUKI (Waseda Univ.), Masato SAKURAI, Mitsuru OHNISHI (JAXA)

1. Introduction

For long stays on board the ISS, it is necessary to reuse/recycle essential materials. Our research group developed a smaller/simpler CO₂ adsorption/desorption device in which zeolite 5A is an adsorbent. The relationship between moisture concentration and $K_F a_v$ was evaluated quantitatively. $K_F a_v$ is an indicator of the effect of moisture on the amount of adsorbable CO₂. We will discuss the acceptable moisture concentration from these results.

2. Experimental Procedure

Experimental apparatus and procedures were based on previous research¹⁾. An adsorption bed with height Z of 0.443 m was used. CO₂ breakthrough experiments were performed with changing moisture concentrations generated by a simple dryer. Concentrations were ranging from 0.5 to 1.2 g/m³, which covers values typically found at the ISS (0.73~1.16 g/m³)²⁾³⁾. The inlet gas velocity u was set at 9.86 m/min. The breakthrough curve was obtained by measuring the time dependence of the ratio of the CO₂ concentrations C (exit) to C_0 (entrance). Experiments were halted as soon as the ratio reached 0.99. The desorption phase was taken for 200 min.

3. Results and discussions

Fig.1 shows an example of a measured breakthrough curve and fitting curve obtained using a least-square method on experimental data. Data was fitted to equation (1)⁴⁾.

$$\frac{C}{C_0} = \frac{1}{2} \left(1 + \operatorname{erf} \left(\frac{\theta - t_0}{2t_0} \sqrt{\frac{u}{K_F a_v Z}} \right) \right) \quad (1)$$

Fig.1 shows that difference between experimental data and fitting is small around $\theta = t_0$, and large around $C/C_0 = 0\sim 0.2$, and $0.8\sim 1.0$. Also, $K_F a_v$ is lower at $\theta < t_0$, than at $\theta > t_0$. It is conceivable that this phenomenon was caused by temperature deviations during the preparatory desorption phase¹⁾.

Fig.2 shows that $K_F a_v$ did not significantly vary with changing moisture concentration. This result shows that the shapes of the breakthrough curves are similar regardless of the moisture concentration in this range.

The total amount of adsorbed CO₂ can be calculated according to equation (1). As $K_F a_v$ values differ only insignificantly at the specified moisture concentrations, these values are the adsorption capacity of the bed. From the results it

is therefore concluded that moisture concentrations in the range of 0.5~1.2 g/m³ have no significant impact on adsorption capacity. The performance of the device will remain stable.

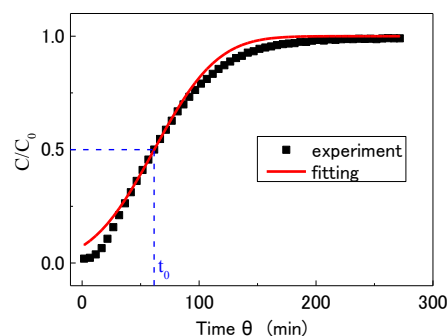


Fig.1 Breakthrough curve and fitting curve (moisture concentration $A=1.10\text{g/m}^3$)

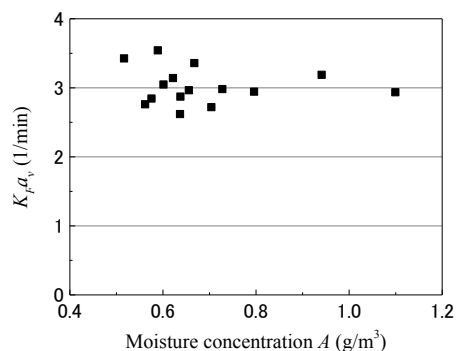


Fig.2 Relationship between $K_F a_v$ and moisture concentration

4. Conclusion

- The parameter $K_F a_v$ does not change significantly with changing moisture concentration.
- The fitting results of equation (1) to experimental data show that $K_F a_v$ is lower at $C/C_0 < 0.5$, than at $C/C_0 > 0.5$. This might be caused by temperature deviations during the preparatory desorption phase.
- In the moisture concentration range of 0.5~1.2 g/m³, our data indicate that the amount of CO₂ adsorption in practical devices will not change significantly.

References

- 1) A. Yokohama, S. Suzuki, M. Sakurai, A. Shima, Int. J. Microgravity Sci. Appl., **30**, 2, 2013, 94.
- 2) P. O. Wieland, NASA Technical Report, 1998-206956, 1998, 59.
- 3) I. Terada, J. Iwamoto, H. Miyake, Membrane, **21**, 5, 1996, 306.
- 4) K. Kawazoe, Y. Takeuchi, J. Chem. Eng. Japan, **7**, 1974, 431.

放射光を用いた液体 Si の動的構造因子の測定

○高橋真人, 北村洗太, 岡田純平 (JAXA), 水野章敏 (学習院大学), 正木匡彦 (芝浦工業大学)

Measurement of Dynamical Structure Factor of Liquid Si by Using Synchrotron Radiation

○Makoto TAKAHASHI, Kouta KITAMURA, Junpei OKADA (JAXA), Akitoshi MIZUNO (Gakushuin Univ.), Tadahiko MASAKI (Shibaura Institute Tech.)

1. Introduction

Recently, the thermo-physical properties of molten materials can be studied experimentally by using the levitation techniques. Especially, the relaxation phenomena, such as viscosity, can be observed with high precision by oscillation droplet method. In addition to that, the levitation techniques make available to study the undercooled liquid state or unstable state of matters. In near future, drop levitation method allows us the observation of material properties with much more high with the application of microgravity environment in space where is the less disturbances caused by gravity on ground.

Form the microscopic points of views, the relaxation phenomena are closely related to the atomic dynamics in liquids. It is well known that the static structure of non-crystalline materials such as liquid metals can be analyzed by X-ray diffraction. Recently, joint using the super photon ring-8GeV(SPring-8), provides us the chance of the observation of the atomic dynamics of matters with the use of the inelastic x-ray scattering (IXS). Then, we can observe the atomic dynamics in undercooled liquids by the combination of IXS and levitation methods.

As the first step for the understanding of atomic dynamics in the undercooled liquid metals, we observed the atomic dynamics of liquid Si by the combination of electrostatic levitation method and the high resolution inelastic X-ray scattering facility in SPring-8.

2. Experimental Method

The spherical sample of Si whose diameter was 2mm was made in glovebox filled with Ar gas. The synchrotron radiation experiment was carried out by the high resolution inelastic X-ray scattering facility at the BL35XU in the Spring-8. The energy of incident X-ray was 21.75keV, and the energy resolution was 1.6meV. Levitation of sample was carried out by an electrostatic levitation furnace which was developed to be able to install in the beamline. The chamber was evacuated to 10^{-5} Pa with a vacuum pumps. As shown in Fig.1, the charged sample between two electrodes was levitated by the electrostatic force due to the

application of high voltage (~ 20 kV) to electrodes. The sample was heated to by two laser diodes. The levitation of samples can be kept for around an hour. Dynamical structure factor $S(Q, \omega)$ was measured during the levitation of sample. The sample temperature was measured by a pyrometer.

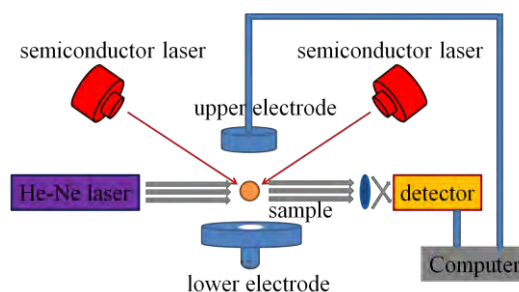


Fig.1 Electrostatic levitation furnace

3. Results and Discussion

The graph in Fig. 2 shows the dynamical structure factor $S(Q, \omega)$ of liquid Si at a temperature close to the melting points, in which momentum transfer, Q , was 4.92 nm^{-1} , and ranges of energy transfer, ω , was $-30 \text{ meV} \sim 30 \text{ meV}$. The elastic peak was observed at the center of spectrum and the inelastic peak was observed at $0 \pm 10 \text{ meV}$. The atomic dynamics of liquid Si will be discussed in the poster session.

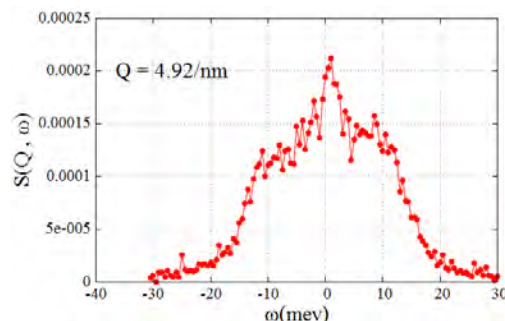


Fig.2 Dynamical structure factor of liquid Si

機能的界面制御剤で調製した W/O エマルジョンの安定性に対する重力場の影響

○山崎貴広 (千葉科学大), 飯島聡, 遠藤健司, 酒井健一, 酒井秀樹, 阿部正彦 (東京理科大), 夏井坂誠 (宇宙航空研究開発機構), 山下裕司, 坂本一民 (千葉科学大・東京理科大)

Effect of Gravity on the Stability of W/O Emulsion Prepared by AIM

○T. YAMAZAKI (Chiba Inst. of Sci.), S. IJIMA, T. ENDO, K. SAKAI, H. SAKAI, M. ABE (Tokyo Univ. of Sci.), M. NATSUISAKA (JAXA), Y. YAMASHITA, K. SAKAMOTO (Chiba Inst. of Sci./Tokyo Univ. of Sci.)

1. Introduction

Emulsion disruption can occur through four processes; creaming, flocculation, coalescence, and Ostwald ripening (Fig.1). Every emulsion goes toward phase separation at equilibrium via one of or multiple routes shown in Fig.1 to achieve minimum interfacial area between water and oil. In spite of wide range of industrial applications, the theoretical understanding on the long-term stability of emulsion has not been well established. Active interfacial modifier (AIM) has unique properties at the water/oil interface due to its extremely lower solubility either in water or in most of organic solvents, in contrast to the common surfactants. Our previous studies revealed that a hybrid amphiphilic polymer (AIM-FN) consisting of a silicone backbone modified with hydrocarbon chains and hydrolyzed silk peptide creates long term stable water-in-oil (W/O) emulsion in the wide composition range of AIM-FN/water/silicone oil (D5) system. For the W/O emulsion using AIM-FN, coalescence hardly takes place even hyper-centrifugal force is applied, although creaming and flocculation are observed. Therefore, the objective of our present study is to investigate the emulsion stability in the AIM-FN/water/D5 system under quasi-microgravity set by 3D clinostat.

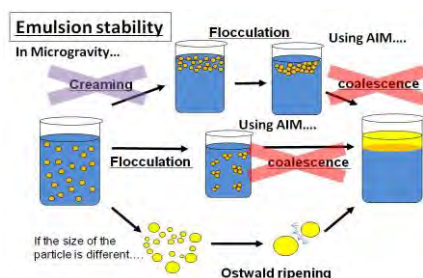


Fig.1 Emulsion disruption processes; creaming, flocculation, coalescence, and Ostwald ripening. (With AIM under microgravity, destabilization factor becomes only Ostwald ripening)

2. Experiment

2.1 Equipment and Stability Evaluation

A 3D clinostat (Mitsubishi Heavy Industries) was used to create time-averaged microgravity. The rotational twin bodies equipped in the 3D clinostat individually turn around in all directions, providing quasi-microgravity environment artificially on ground. The recent study reported that the device can attain a microgravity environment of $1 \times 10^{-3}G$ [1].

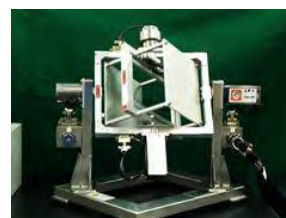


Fig.2 3D Clinostat

The stability of emulsion was evaluated under hyper-centrifugal force and quasi-microgravity in the clinostat. The emulsion droplet size and phase separation degree were measured as the stability factors by visual and microscopic observations, respectively.

2.2 Materials and Emulsion Preparation

Hydrolyzed silk PG-propyl methylsilanediol crosspolymer (AIM-FN) was used as AIM. A commercial silicone emulsifier (KF-6038; lauryl PEG-9 polydimethylsiloxyethyl dimethicone, Shin-Etsu Chem. Co., Ltd) was used as a reference. Decamethyl cyclopentasiloxane (D5, Dow Corning Toray Co., Ltd) was used as oil and ultrapure water ($\rho > 18M\Omega \cdot cm$) was used.

AIM-FN or KF-6038 was dispersed in D5 at 70 °C, then water was added under voltxmimer agitation or by thin-film spin mixer (Filmix®, PRIMIX Co.) to obtain an emulsion.

3. Results and Discussions

The emulsion creaming stability is accelerated by hyper-centrifugal force according to the Stokes law expressed as a function of the density difference of water-oil ($\Delta\rho$) and the viscosity of the continuous phase (η), and the size of the dispersed phase (d). The phase separation (W/O+O) was observed under hyper-centrifugal force regardless of $\Delta\rho$ and η modulated for different oils. Although creaming followed Stokes law, there are no coalescence observed for three oils and sizes and distributions of particle are kept un-effected by hyper-centrifugal force. Hence, for the emulsion with AIM destabilization factor becomes only Ostwald ripening under microgravity. In our presentation, we will show further results on the emulsion stability under quasi-microgravity in the 3D clinostat and discuss the gravitational effect on the deterioration kinetics of emulsion.

[1] N. Komatsu et. al, Mitsubishi Heavy Ind. Tech. Review, Vol.35, No.5 (1998)

微小重力環境下における液柱マランゴニ対流の不安定性に与える 表面からの熱授受の影響

○田崎倫之（筑波大院），松本聡（JAXA），鴨谷康弘（ケースウェスタン大），西野耕一（横浜国立大）
上野一郎（東京理科大），小宮敦樹（東北大），今石宣之（九州大），矢野大志（横浜国立大院）
金川哲也（筑波大），金子暁子（筑波大），阿部豊（筑波大）

Influence of Heat Transfer at Free Surface on Instability of Marangoni Convection in Liquid Bridge under Microgravity Condition

○Michiyuki Tasaki (University of Tsukuba), Satoshi Matsumoto (JAXA),
Yasuhiro Kamotani (Case Western Reserve University), Koichi Nishino (Yokohama National University),
Ichiro Ueno (Tokyo University of Science), Atsuki Komiya (Tohoku University),
Nobuyuki Imaishi (Kyushu University), Taishi Yano (Yokohama National University),
Tetsuya Kanagawa (University of Tsukuba), Akiko Kaneko (University of Tsukuba),
Yutaka Abe (University of Tsukuba)

1. Introduction

As is well known, the Marangoni convection, it is classified as natural convection same buoyancy convection due to density difference. There is a driving force only on the surface to Marangoni convection. Surface tension is the power to reduce the surface area. In general, surface tension, when the temperature difference exists along the surface becomes stronger with decreasing temperature, and the convection is generated surface is pulled in the low temperature region. Flow is steady when the temperature difference is small, but the flow is transition to the oscillatory flow to be above a certain temperature difference¹⁾. Although this transition point is intensively affected by the heat transfer²⁾, the reason is unclear. The purpose of this study is elucidation of the influence of heat transfer on the oscillating flow generation mechanism.

2. Experiment

Figure 1 depicts the schematic diagram of the experimental apparatus. We visualized from the side and upward. The constant temperature cold disk to see the effect of heat loss has on the oscillatory flow transition and allowed to transition the flow raises the temperature of the heating disk in this study. Transition point was determined from the temperature oscillation by a short period of time FFT analysis. Figure 2 shows described the dependency of cold disk temperature on the critical Marangoni number, Ma_c . Furthermore, Cold disk has decreased around 24 degrees, and that the critical Marangoni number is different to three times. However, the critical Marangoni number is hardly changed for the case that cold disk temperature exceeds 24 degrees. The increase of cold disk temperature represents an increase of heat loss from the liquid bridge. Thus the critical Marangoni number is influenced by

heat loss from the surface of the liquid bridge. We discussed the influence of heat loss from the results of this experiment.

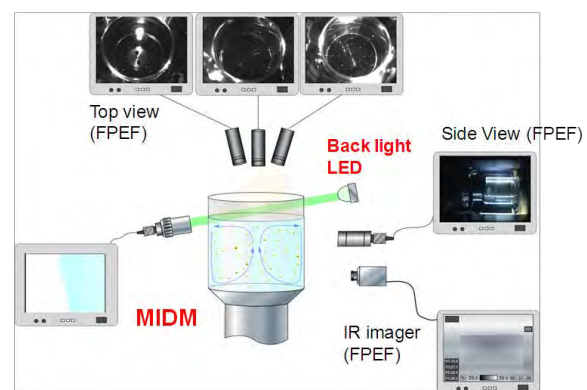


Fig. 1 Experimental apparatus

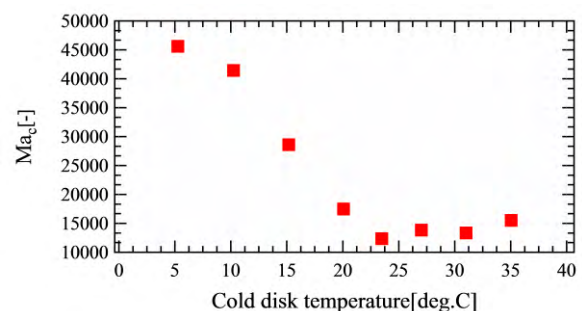


Fig. 2 Critical Marangoni number

References

- 1) Preisser, F., Schwabe, D. & Scharmann, J. Fluid Mech. **126**, 545-567, 1983.
- 2) Kamotani, Y., Wang, L., Hatta, S., Selver, R., & Yoda, S., J. Jpn. Soc. Microgravity Appl. **18**, 283-288, 2005.

自己組織化微細構造形成時の対流の構造に与える影響

○井内健豊, 平井悠司, 下村政嗣 (千歳科技大), 夏井坂誠 (JAXA), 今石宣之 (九大), 辻井薫 (中央大)

Effects of Convections for the Formation of Self-Organized Microstructures

○Kento IUCHI, Yuji HIRAI, Masatsugu SHIMOMURA (CIST), Makoto NATSUISAKA (JAXA), Nobuyuki IMAISHI (Kyushu Univ.), Kaoru TSUJII (Chuo Univ.)

1. Introduction

We have reported microporous polymer films can be prepared by casting a solution of hydrophobic polymer and amphiphilic polymer on a solid substrate by using condensed water droplet arrays as templates¹⁾. In this preparation method, evaporation cooling induces the condensation of water droplets, which act as templates of micropores, on the solution surface. However, some defects of pore arrangement are generated by thermal convection arising from a temperature difference between the surface and the bottom of the solution²⁾. By preventing the thermal convection, better films where the micropores are well ordered like single crystalline can be obtained. Herewith, we investigate the origin of thermal convections by the shadowgraph method.

2. Experiment

A photograph of experimental setup is shown in Fig. 1. Five ml of a chloroform solvent (control) and a chloroform polymer solution containing polystyrene and amphiphilic copolymer¹⁾ were casted on petri dishes, respectively. After casting the solutions, humid airflow was blown to the solution surfaces through a funnel. By illuminating the solution with a point light source, gradation of shadow reflecting differences in refractive indexes at local positions is projected on the screen. The solution weights were also measured in the same condition to calculate the thicknesses of the solutions.

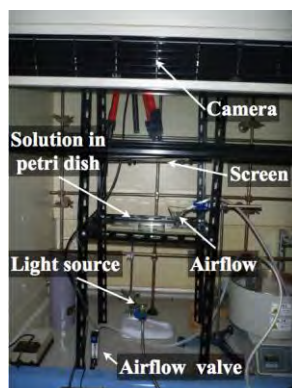


Fig. 1. A photograph of experimental setup

3. Results and Discussion

Fig. 2 shows a series of the shadowgraphs for the cases with or without polymers. The convective patterns induced by thermal differences were clearly visualized. The convective pattern sizes were almost the same at the same timing, and gradually reduced with time passing. In order to check if the convection is really caused by the evaporation, it was stopped by covering with a lid and it was confirmed that convective patterns were disappeared.

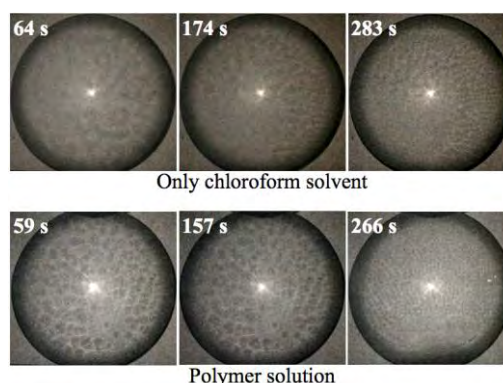


Fig. 2. Shadowgraphs obtained during solvent evaporation

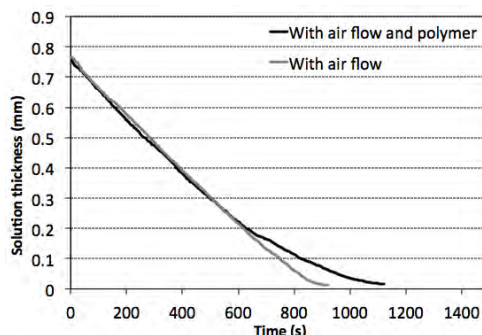


Fig. 3. A graph of solution thickness

Fig. 3 shows the solution thicknesses calculated from the solution weights. The decreasing rates were almost the same for the both cases, but in the case of “with polymer”, the rate was getting slower after 600s. This is because the surface of the solution was covered with the condensed water droplets and the solvent evaporation became difficult. (In case of only chloroform solvent, water condensation was not occurred).

4. Summary

We successfully obtained shadowgraphs indicating convective flow patterns during a microporous polymer film formation as shown above. We plan to investigate the effect of addition of polymers and/or water droplets on the convective patterns as further investigations to find a condition that can eliminate a natural convection and provide better films.

References

- 1) H. Yabu, Y. Hirai, M. Shimomura: *Langmuir*, **22**, (2006) 9760
- 2) H. Yabu, Y. Hirai, M. Shimomura, M. Natsuisaka, and K. Tsujii: *Jpn. J. Appl. Phys.*, **49**, (2010) 110210

空気圧パワーアシストを用いた宇宙活動での関節機能向上

○谷嶋 信貴, グバレビッチ アンナ, 和田 裕之, 小田原 修 (東工大)

Improvement of Joint Function in Space Exploration Activities by Pneumatic Power Assist

○Nobutaka TANISHIMA, Anna GUBAREVICH, Hiroyuki WADA, Osamu ODAWARA
(Tokyo Institute of Technology)

1. Objectives

Pressure conditions of spacesuits applied to ISS activities have been designed to decrease to around 0.3 atm as inner pressure, which should require at least 150 minutes for denitrogenation to prevent decompression sickness of astronauts. This means that astronauts cannot start their extra vehicular activity quickly after attaching spacesuits. If emergent maintenance is needed, the inner pressure of 0.58 atm would be suitable for prompt activity. Therefore, designs of next generation spacesuit should be higher than 0.58 atm would make extra vehicular activity more efficient. However, larger gap of air pressure between inside and outside of the spacesuit causes cloth expansion as balloon, resulting in extra torque for joint bending.

In this study, application of pneumatic power is proposed to improve flexibility of joint. The ideas shown in this presentation have been selected by considering space environment, elasticity and flexibility as human muscle.

Fig.1 shows the torque calculated for the arm joint angle with 0.6atm inner air pressure using following formula (1).

$$N=L\pi r^2\Delta P\sin\theta \dots(1)$$

N: Torque (N·m), r: Joint radius (m), θ: Arm joint angle (°)
L: Arm length (m), ΔP: Inner pressure (Pa).

From Fig.1, maximum torque of 13.3N·m is required when the arm joint angle is 90°. Therefore, the present achievement of torque is focused at least more than 13.3N·m. Judging from the design with human muscle-like motions, response speed should be also less than 0.1 second.

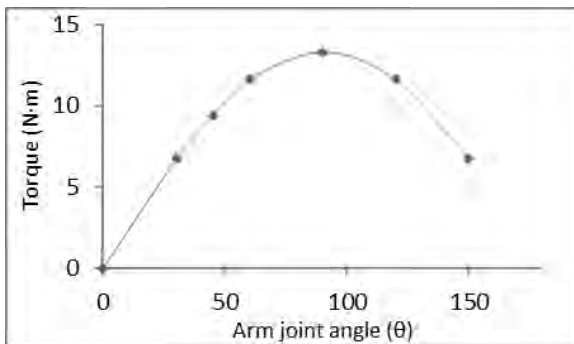


Fig.1. Torque for the arm joint angle (r = 0.075m)

2. Actuator design (rubbertuator)

The present actuator contracts and expands with compressing air. Structure and mechanism of the rubbertuator is shown in Fig.2. Rubbertuator is made from rubber tube covered with fiber cord. Metal fittings at each end permits the entry and exit of compressed air.

Pneumatic power source is the most typical character of the rubbertuator. This enables rubbertuator to contain contract element, spring element and dumper element as human muscle.

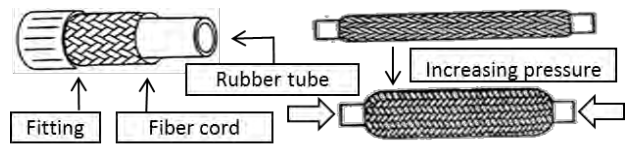


Fig.2. Structure and mechanism of rubbertuator

3. Experimental

Experimental procedures are carried out with the following steps: to pressurize the air tank (0~5 atm), to open the gate valve to activate the rubbertuator (5mm, 10mm, 20mm in inner diameter), to close the gate valve and decompress the air tank.

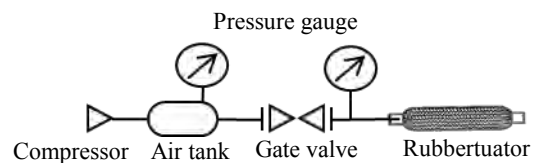


Fig.3. Experimental equipment

4. Results

Figs.4 and 5 show rubbertuator's performances. From the present results, the rubbertuator has started the elastic deformation from 1 atm in pressure difference. Its spring constant increases as the inner pressure increase.

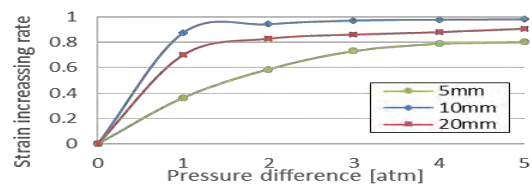


Fig.4. Strain increasing rate

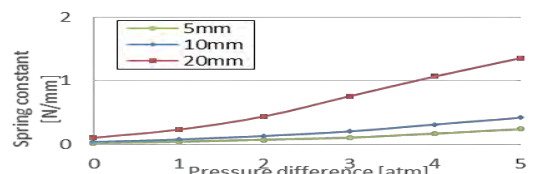


Fig.5. Spring constant

静電浮遊液滴の回転分裂時における界面変形と内部流動挙動

○綿引壮真 (筑波大院), 松本聡 (JAXA), 金川哲也, 金子暁子, 阿部豊 (筑波大学)

Interfacial Deformation and Internal Flow Behaviors during Rotational Breakup of Electrostatic Levitated Droplet

○Soma WATAHIKI (University of Tsukuba), Satoshi MATSUMOTO (JAXA), Tetsuya KANAGAWA, Akiko KANEKO, Yutaka ABE (University of Tsukuba)

1. Introduction

By using the electrostatic levitation method, it has become possible to measure thermophysical property of a high melting point sample without container¹⁾. However, there was no method to measure viscosity in range from 0.1 to 100 [Pa·s]. Our group has proposed a new method to measure the viscosity of the sample within this range²⁾. Our method utilizes rotational breakup behavior of the droplet, and the measurement error is about 30% until now. In this study, internal flow during the rotational breakup was investigated, and the effect of non-axisymmetry and mean curvature of the droplet on the measurement result was evaluated.

2. Experimental method

The experimental apparatus is illustrated in Fig. 1. Two cylindrical electrodes were placed vertically opposite. Conductive glass window was fixed on the bottom of the upper electrode. The acrylic needle jig was filled inside the bottom electrode. The injection needle is inserted through the hole in the acrylic fixing. The droplet was formed at the tip of the needle. The droplet was charged electrically since the needle was connected to a power supply. When a negative high voltage was applied to the upper electrode, the droplet was levitated in the air by electrostatic force. The vertical position of the droplet was detected by using the He-Ne laser and the position detector, and controlled by adjusting the voltage of the upper electrode through the PID algorithm. The electrodes were placed in the acrylic chamber. The droplet was rotated by acoustic torque generated by a pair of orthogonal positioned loudspeakers attached on the side wall of the chamber³⁾. The rotational breakup behavior of the levitated droplet was observed by using two high-speed video cameras and two metal halide lamp. The images were taken from both upper and side of the droplet. To observe the internal flow, the fluorescent particles were mixed in the test fluid in advance. The particles on the horizontal plane of the droplet were fluorescent by sheeted laser beam generated by Nd:YAG laser and cylindrical lens. The experiments were performed in normal pressure at room temperature. The test fluid was Glycerol (density 1260 [kg/m³], surface tension 63 [mN/m], and viscosity 1.0 [Pa·s]).

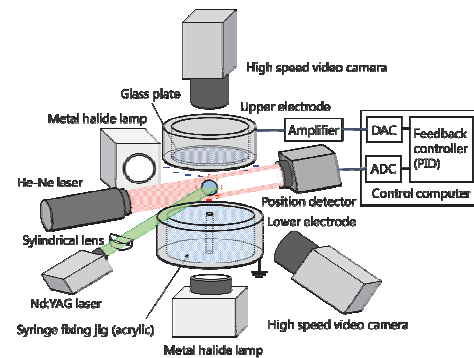


Fig. 1 Schematic diagram of electrostatic levitator

3. Results and discussion

3.1 Rotational breakup behavior

Figure 2 shows the observation results of rotational breakup of the levitated droplet. Time of 0 [ms] indicates the moment of breakup. The droplet was elongated and the midpoint diameter became smaller as the output power of the loudspeakers increased. Finally, the midpoint of the droplet was pinched off. In the side view images (a) ~ (c), we found that the midpoint of the droplet was a non-axisymmetric shape slightly. In the image (d), the droplet was an axisymmetric shape. In the image (e), the midpoint of the droplet was significantly distorted upward. In the image (f), the droplet was broken up and a satellite droplet was generated.

3.2 Internal flow

The trajectories of the tracer particle in the droplet just before rotational breakup for 11.33 [ms] were shown in Fig. 2; white arrows show the direction of each particle. Figure 3 shows time series of the velocities of each particle in the axial and radial directions. Each color corresponds to the color of the particles in Fig. 2. As a result, flow velocity in the radial direction around the midpoint of the droplet was constant, on the other hand, flow velocity in the axial direction increased with axial distance from the midpoint (Fig. 4).

3.3 Viscosity calculation

The stress balance at the midpoint of the droplet during rotational breakup²⁾ was modified in the viewpoint of mean curvature. The modified stress balance is expressed by,

$$3\eta_s \left\{ -\frac{2}{D_{mid}} \left(\frac{dD_{mid}}{dt} \right) \right\} = \frac{2mr\omega^2}{\pi D_{mid}^2} - \frac{2\sigma}{D_{mid}} H_{mid}, \quad (1)$$

where η_s , D_{mid} , m , r , ω , σ , and H_{mid} are the viscosity, midpoint diameter, mass of the droplet, length between center and center of gravity in one side of the lobe, angular velocity, surface tension, and mean curvature, respectively. In the each term of the eq. (1), the left-hand side, the first and second terms of the right-hand side indicate the viscous stress, centrifugal stress, and surface tension stress, respectively. The corrective coefficient by mean curvature $H_{mid}^{(4)}$ is given by

$$H_{mid} = \left\{ \frac{1}{\sqrt{1 + (R(z)')^2}} + \frac{R(z)R(z)''}{(\sqrt{1 + (R(z)')^2})^3} \right\}_{z=0},$$

where $R(z)$ is the distance from long axis of the droplet to interface. The edge pixel of the droplet interface is obtained via Canny edge detector algorithm. The edge pixel is approximated by a hyperbolic cosine function to obtain $R(z)$. Furthermore, left term except viscosity η are moved to right side, eq. (2) to calculate viscosity is derived.

$$\eta = \frac{(mr\omega^2/\pi D_{mid}) - \sigma H_{mid}}{-3(dD_{mid}/dt)}, \quad (2)$$

Figure 5 shows the value of each term of the eq. (1) and calculated viscosity by eq. (2). The centrifugal stress term surpasses the viscous and surface tension stress terms just before the breakup, and in this regime, the surface tension stress term is much smaller than others. By correcting the surface tension term by mean curvature, the value of surface tension term increased slightly. The effect of mean curvature of the droplet became smaller as the droplet approached breakup. In axisymmetric regime, the result of the viscosity calculation was closer to the appropriate value with actual viscosity.

4. Conclusion

- (1) Flow velocity in the radial direction around the midpoint of the droplet was constant, in the axial direction increased with the axial distance from the midpoint during rotational breakup of the droplet.
- (2) When the droplet was an axisymmetric shape, the result of viscosity measurement showed appropriate value as actual viscosity.
- (3) The effect of mean curvature of the droplet became smaller as the droplet approached breakup.

References

- 1) T. Ishikawa, J. T. Okada, P.-F. Paradis, Y. Watanabe: International Journal of Thermophysics, **31** (2010) 388.
- 2) R. Tanaka, S. Matsumoto, A. Kaneko, Y. Abe: Interfacial Phenomena and Heat Transfer, **1** (2013) 181.
- 3) F. Busse, T. G. Wang: The Journal of the Acoustical Society of America, **69** (1981) 1634.
- 4) P. Szabo: Rheologica Acta, **36** (1997) 277.

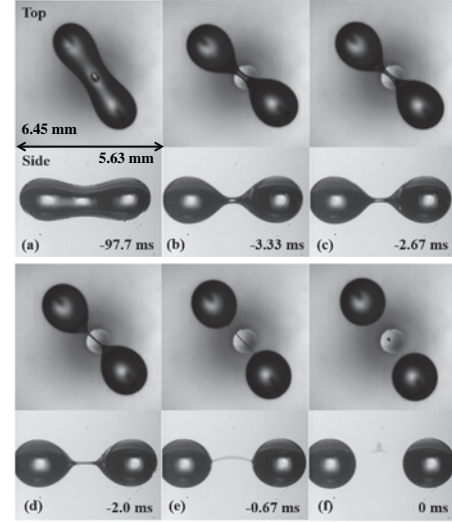


Fig. 2 Top and side views of the levitated droplet during rotational breakup

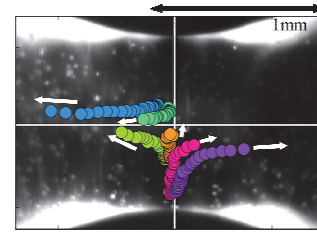


Fig. 3 The trajectories of the typical tracer particles

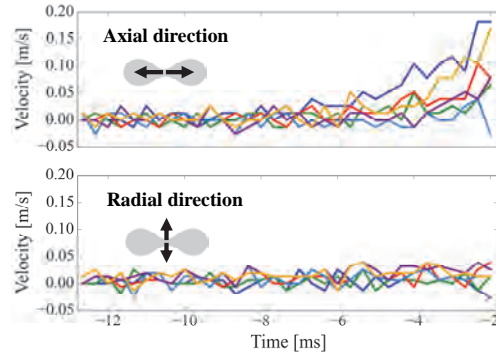


Fig. 4 Time series of the velocity of each particle in axial and radial direction

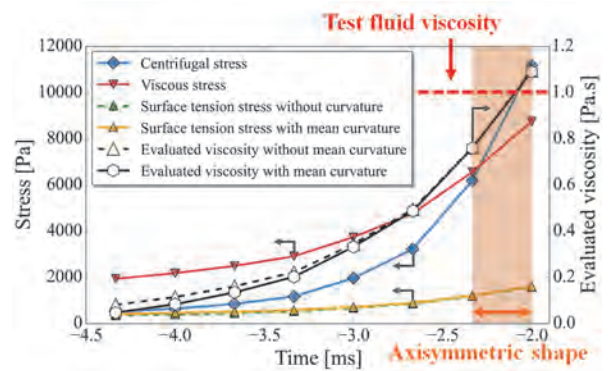


Fig. 5 Time series of each stress acting on the levitated droplet central part and estimated viscosity

ISS を利用したソーレ係数測定方法の改善

○長田拓真, 橋本栄堯, 鈴木進補 (早大), 稲富裕光 (JAXA/ISAS)
伊藤裕一 (JAXA), 島岡太郎 (JSF)

Improvement of measuring method for Soret coefficient on the ISS

○Takuma OSADA, Yoshitaka HASHIMOTO, Shinsuke SUZUKI (Waseda Univ.)
Yuko INATOMI (JAXA/ISAS), Yuichi ITO (JAXA), Taro SHIMAOKA (JSF)

1. Introduction

Recently, we performed experiments of “Soret-Facet” on the International Space Station (ISS) to measure accurate Soret coefficients S_T ¹⁾. An effective correction method for thermal expansion of a quartz glass cell has already been established by subtraction of the moving distance of interference fringes in the wall side from those in solution side²⁾. Therefore, the measurement results of “Soret-Facet” on the ISS should be corrected by this method. The validity of the correction method was confirmed with interference fringes with aligned in the parallel direction to a temperature gradient (vertical fringes, //).

However, the quartz glass cell on the ISS “FACET-cell” has so thin wall for observation to set enough amount of fringes for a high resolution for accurate S_T . Therefore, interference fringes with aligned in vertical direction to a temperature gradient (lateral fringes, ⊥) were used in the “Soret-Facet”. The lateral fringes have advantages that a proper amount of fringes can be set with a high resolution even in the thin wall. On the other hand, the lateral fringes require an additional correction for variation of distance between fringes during change of temperature and concentration.

We checked the validity of the correction method for the lateral fringes in the ground experiments by comparing with the result of vertical fringes. And we discussed the difference of S_T values between with and without the correction of thermal expansion of FACET-cell.

2. Experimental Procedure

2.1 Ground Experiments

We measured S_T of salol – 9 mol% *tert*-butyl alcohol solution by a two-wavelength Mach-Zehnder interferometer with wavelengths λ of 532 nm and 780 nm. Fig.1 shows a schematic illustration of the two-wavelength Mach-Zehnder interferometer. Then, thermal expansion of the quartz glass cell was corrected to measure accurate S_T . In the ground experiment, S_T were measured by using both vertical and lateral fringes.

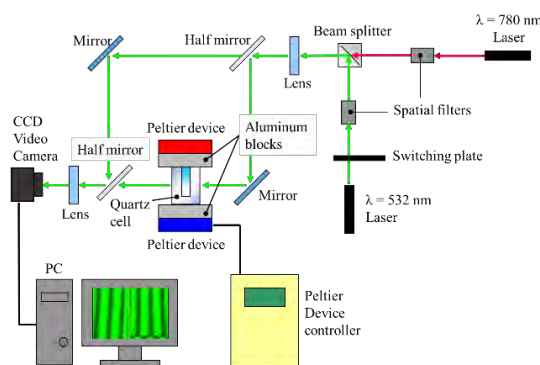


Fig.1 Schematic illustration of the two-wavelength Mach-Zehnder interferometer²⁾

The center of the observation window was set 2 mm upper from the bottom side. Setting temperature program is shown in Fig.2. At first, both top and bottom sides of the cell were heated up and kept at 50 °C with Peltier devices for over 24 h (homogenization time t_h). The mirrors were adjusted so that the interval of dark lines were about 30 pixels (532 nm) and about 48 pixels (780 nm) in the solution side during homogenization time for both vertical and lateral fringes. The movies of the interference fringes were recorded for 21 h (Soret effect time t_{soret}) just before the temperature of the bottom side was lowered from 50 to 40 °C.

Number of crossing dark lines on the observation point was measured to obtain the moving distance of interference fringes. We subtracted the moving distance of interference fringes in the wall side from those in solution side to correct thermal expansion of a quartz glass cell²⁾. The variation of distance between fringes was corrected in the experiment using lateral fringes.

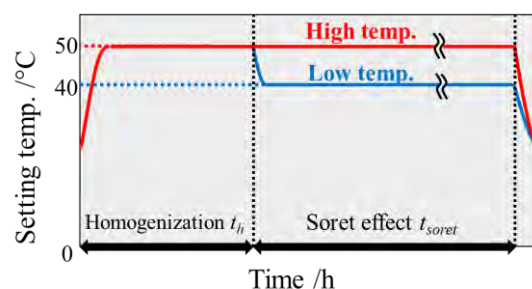


Fig.2 Setting temperature program of Peltier devices

2.2 ISS Experiment

We measured S_T of salol - *tert*-butyl alcohol solution by Solution Crystallization Observation Facility (SCOF) equipped with the two-wavelength Mach-Zehnder interferometer. The concentration of *tert*-butyl alcohol was about 3 mol%. Setting temperature program was equal to Fig.2. Homogenization time t_h was 7 h and Soret effect time t_{soret} was 10 h. The mirrors were adjusted for lateral fringes during homogenization time. The center of the observation window was set 1 mm under from the center of FACET-cell.

3. Results and Discussion

Fig.3 shows the pictures of lateral and vertical fringes in 1g and μg . The areas surrounded with the red frames are the cell walls. The measured values of S_T obtained in 1g are $4.4 \pm 0.46 \times 10^{-2} \text{ K}^{-1} (//)$ and $3.8 \pm 0.44 \times 10^{-2} \text{ K}^{-1} (\perp)$, which agreed each other. A proper amount of lateral fringes can be set with a high resolution even in the thin wall of FACET-cell under μg by using lateral fringes.

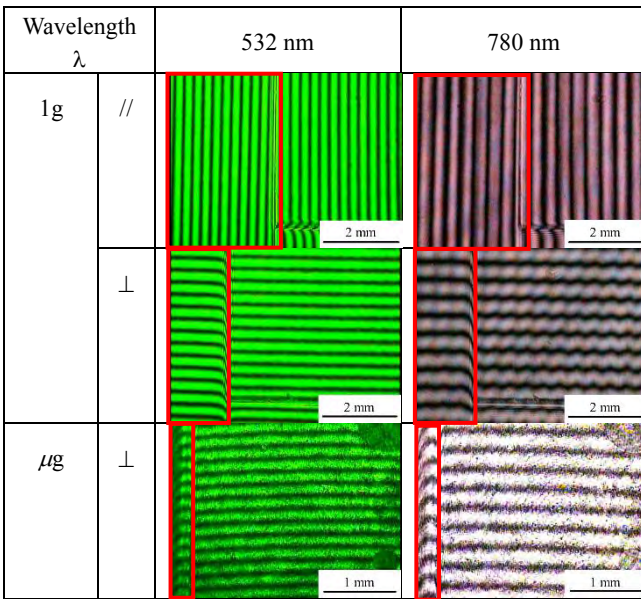


Fig.3 Vertical and lateral fringes in 1g and μg

Fig.4 shows number of crossing dark lines in the solution side and the wall side against time under μg ((a)532 nm, (b)780 nm). As shown in Fig.4, the fringes in the wall side move by thermal expansion of FACET-cell. Therefore, it is necessary to subtract the moving distances of interference fringes in the cell wall side from those in the solution side. The maximum difference of the obtained S_T values between with and without correction was 70 % of the S_T value with correction. Therefore, the correction is necessary for accurate measurements of S_T to eliminate the error of thermal expansion under μg .

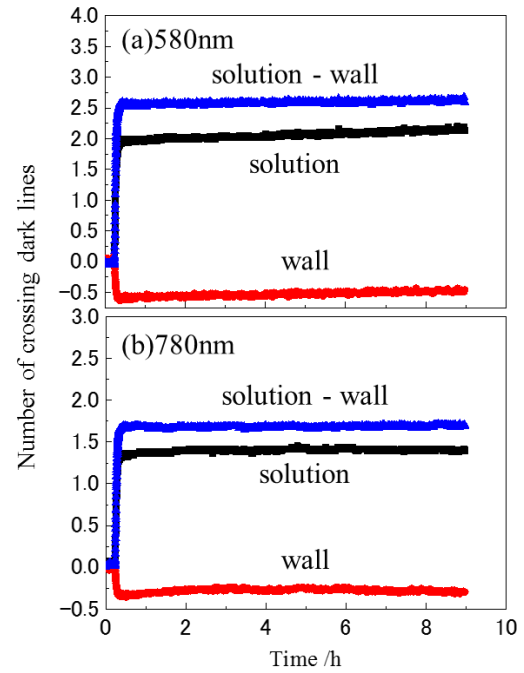


Fig.4 Number of crossing dark lines against time under μg of 532 nm (a) and 780 nm (b)

4. Conclusions

We compared the result of lateral fringes with vertical fringes. The validity of the correction method for the lateral fringes was confirmed in the ground experiments. The lateral fringes were used in the “Soret-Facet” and thermal expansion of FACET-cell can be corrected without reducing resolution. And the maximum difference of the obtained S_T values between with and without correction was 70 % of the S_T value with correction. Therefore, the correction is necessary for accurate measurements of S_T to eliminate the error of thermal expansion under μg .

Acknowledgments

The authors are deeply grateful to Japan Manned Space Systems Corporation (JAMSS) for the operation of the payloads of the ISS experiments.

References

- 1) S. Suzuki, Y. Mori, Y. Hashimoto, Y. Inatomi, T. Masaki, M. Watanabe, A. Mizuno, I. Ueno, T. Yamane, T. Itami, M. Katsuta: J. Jpn. Soc. Microgravity Appl., JASMAC27 (2013) B08.
- 2) Y. Mori, Y. Hashimoto, S. Suzuki, Y. Inatomi: Transactions of JSASS, in press.

ソーレ効果に及ぼす各因子の影響
~ISS と地上における 2 波長干渉計を用いた測定~

○橋本栄亮, 長田拓真, 鈴木進補 (早大), 稲富裕光 (JAXA/ISAS), 勝田真登 (JAXA),
島岡太郎(JSF)

Influence of Parameter on the Soret Effect

~Measurements using Two-wave Length Interferometer on the ISS and the Ground~

Yoshitaka HASHIMOTO, Takuma OSADA, Shinsuke SUZUKI (Waseda Univ.), Yuko INATOMI (JAXA/ISAS),
Masato KATSUTA (JAXA), Taro SHIMAOKA (JSF)

1. Introduction

The Soret effect plays an important role in solidification and crystal growth processing operations, and so on. This parameter, which is called the Soret coefficient S_T is described by the following equation.

$$S_T = -\frac{1}{C_0(1-C_0)} \frac{\Delta C}{\Delta T} \quad (1)$$

Here, C_0 and $\Delta C/\Delta T$ are the average concentration and the ratio between the concentration and the temperature gradients at the steady state, respectively. However, accurate measurement of the temperature and the concentration is difficult, so the amount of reliable data of S_T is too small to discuss the temperature dependence of S_T .

In this study, we investigated S_T under the 1g and the μg conditions. The convection-free μg conditions were realized in Kibo/ International Space Station (ISS).

2. Experimental procedure

In the 1g and the μg experiments, the samples were prepared by adding 6 and 3 mol% *tert*-butyl alcohol to the molten pure salol and packed in a quartz cell, respectively. Then, we investigated S_T by using a Mach-Zehnder interferometer with two lasers of wavelengths of 532 nm and 780 nm²⁾ on the two experiments. And we investigated S_T by using Solution Crystallization Observation Facility (SCOF)/Kibo under μg conditions, also.

Both top and bottom sides of the cell were heated at the same temperature by Peltier devices. After the temperature of the sample achieved steady state, the bottom side was set 10 K lower than the upper side which was kept at the constant temperature. Then the interference fringes shifted because of refractive index change. The variations of ΔT and ΔC were calculated from shift of interference fringes measured from the initial homogenization states²⁾.

3. Results and discussion

The measured ΔC showed that the concentration decreased in the lower temperature side after setting a temperature gradient

under the μg conditions, although it increased under 1g. Following reasons are considered for the difference between the results obtained in 1g and μg .

The neutral point of flow of *tert*-butyl alcohol should exist in the middle between the top and the bottom. However, the neutral point might have shifted to the higher temperature side in the μg experiments after setting a temperature gradient. In this case, the flow direction of *tert*-butyl alcohol agrees each other between 1g and μg experiment.

On the other hand, there is a possibility that the flow direction of *tert*-butyl alcohol is different between 1g and μg experiments. Since the S_T value itself is an intrinsic property of a solution system, it is independent from the gravity condition. Therefore, additional mass transport can be considered in 1g experiment, such as buoyancy flow.

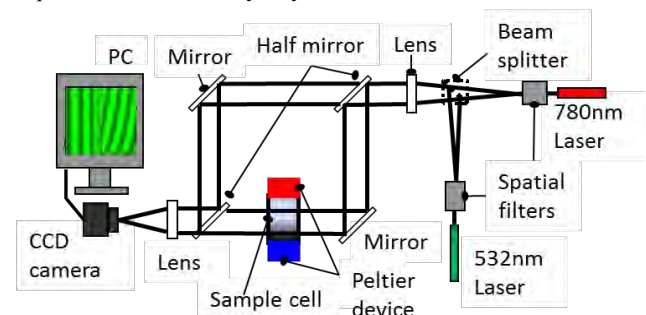


Fig.1 Schematic illustration of the Mach-Zehnder interferometer

Acknowledgments

The authors are deeply grateful to Japan Manned Space Systems Corporation (JAMSS) for the operation of the payloads of the ISS experiments.

References

- 1) Y. Inatomi, I. Yoshizaki, K. Sakata, T. Shimaoka, T. Sone, T. Tomobe, S. Adachi, S. Yoda and Y. Yoshimura: Defect and Diffusion Forum, **323-325** (2012), 533-537.
- 2) Y. Mori, Y. Hashimoto, S. Suzuki, and Y. Inatomi, Transactions of the JSASS, in press.

斜面を用いた低重力装置の開発：斜面摩擦力への対策

○伴野貴哉, 中村祐二 (豊橋技科大), 関本孝三 (関本技術事務所), 野田進 (豊橋技科大)

Development of Low-gravity Generator vis Slope-sliding Method: Strategy to Minimize Wall Frictional Force

○Takaya BANNO, Yuji NAKAMURA (Toyohashi Univ. Tech.), Kozo SEKIMOTO (Sekimoto PE), Susumu NODA (Toyohashi Univ. Tech.)

1. Introduction

Living in low gravity environment is a keyword for future manned mission to outer space environment. Although a number of series of microgravity research projects have been made and fundamentals on microgravity effect on various science fields have been known, we only come to know the microgravity effect and the partial gravity effect is still open question. For instance, it is difficult to answer immediately following questions; what happens if the human being is exposed on to the partial gravity field in long term; what is the critical gravity to be eligible for our body to adopt (adjust) naturally? In order to study such issue, development on a facility to generate the low gravity environment on the earth is highly demanded.

Previously, we have proposed the concept of “low-gravity generator” by using the sliding over the frictionless (ideal) slope; named SSMe (Slope Sliding Method) (See Fig.1)¹⁾. According to the demonstration, the concept seems to work, however, there must be special treatment on the sliding surface to eliminate the frictional loss. Since it is obvious that the surface treatment can relax the friction but fail to eliminate it, there must be another way to introduce external force to compensate it. Here, we study the possibility to eliminate the frictional force effectively with high-controllability by using pulley-drag mechanism. Although demonstration test is underway and not ready at present, the design concept shall be introduced.

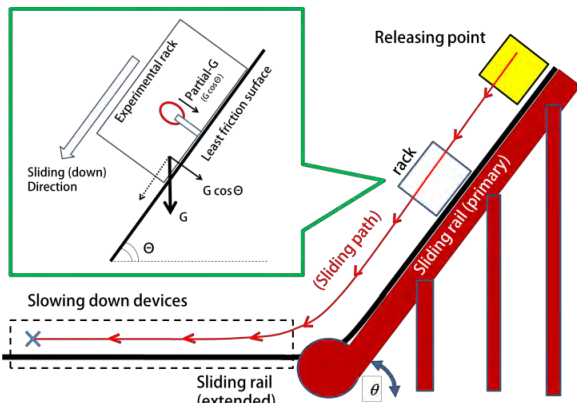


Fig. 1. Schematic illustration of the concept of slope-sliding method (SSMe)¹⁾

2. Target of Revision

2.1 Brief Introduction of SSMe

Although the detail description of the concept of SSMe has been available in elsewhere¹⁾, a brief introduction will be made here for reader’s convenience. SSMe is handy, less-cost, low-gravity generator by using slope-sliding concept. Consider the candle flame is formed in the box. When the box with candle is sliding over the frictionless slope (whose angle of θ), the flame does not feel any acceleration in the direction of sliding, however, the normal component of gravity ($G \cdot \cos \theta$; G is gravity acceleration, m/s^2) on the slope surface is only acceleration for the flame to be experienced. Thus any partial gravity environment can be created in the box once we control the angle of the slope.

Although the concept and structure are simple enough, technical difficulty is how to treat the residual acceleration along the sliding direction caused by the frictional force between the box and the slope, as discussed in our previous work¹⁾. If it is possible to eliminate the acceleration component along the sliding direction (namely, in the direction the box is freely drops), only the normal direction of gravity component against the slope surface is remained.

2.1 Actual Frictional Force to be Compensated

As shown in Fig.2, $\mu' MG \cos \theta$ (M : mass of the box, kg) is the force to be compensated. According to the previous demonstration¹⁾, by using plastic board spread with chalk powder, estimated coefficient of kinetic friction (μ') is 0.176. Importantly, this force to be compensated is constant value during the sliding event once the slope angle is fixed. Namely, some external force to compensate this much shall be introduced to fulfill the demand.

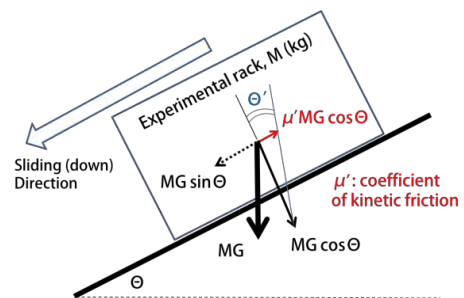


Fig. 2. Actual force balance subjected to the rack the sliding operation¹⁾

2.2 Candidate Concept: Introducing the Constant Drag Force toward the Sliding Direction

Since the target is “constant” force (or constant acceleration) in the direction of sliding, one simplest candidate is to add corresponding (constant) drag force. Simplest way to achieve this purpose, the following concept might work as shown in Fig.3, namely, the constant force is induced by the falling counter weight.

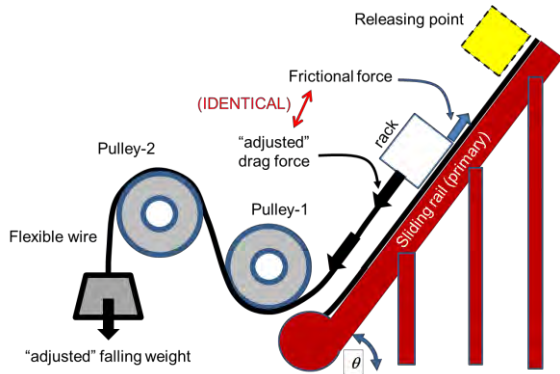


Fig. 3. Schematic illustration the system to introduce the constant drag force via falling “adjustable” weight

By adjusting the (counter) falling weight, the frictional force between the slope and the rack shall be compensated. However another difficulty (ambiguity) should arise by this concept, namely, the additional frictional force between the pulleys and the flexible wire must be considered. To avoid this problem, introducing the active control on drag force (not passive control as shown in Fig.3) sounds reasonable.

2.3 Active Control of Drag Force by Introducing Torque-adjustable Motor

The schematic illustration of suggested active control system is depicted in Fig.4.

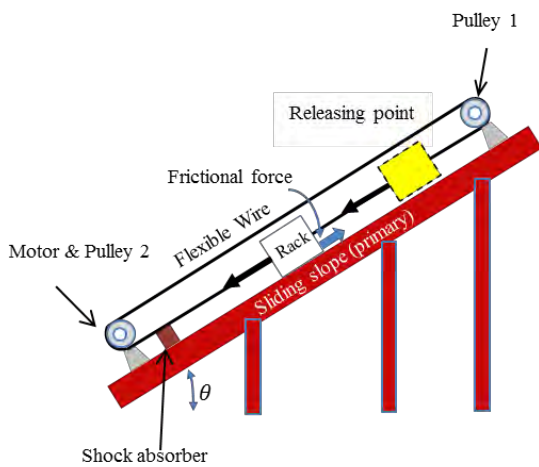


Fig. 4. Schematics of active control system to compensate the frictional force

As shown in this figure, motor is installed to roll-up the wire, just likely belt-conveyer system. The motor has sensor to control the torque to maintain the constant drag force. In this way, the constant drag force is easily obtained to compensate the prescribed frictional force in the system assisted by torque-control circuit.

Let us briefly estimate how it works. First consider the following conditions to estimate the necessary torque-controlled performance under specific design of the system

- μ (coefficient of friction) < 0.1
- m (mass of the sliding rack) > 0.5 kg
- R (radius of pulley) > 0.01 m
- θ (angle of slope) = $\pi/6$ (arbitrary determined)

For given slope angle, it is estimated the necessary torque to be controlled and the brief results are given in Fig.5.

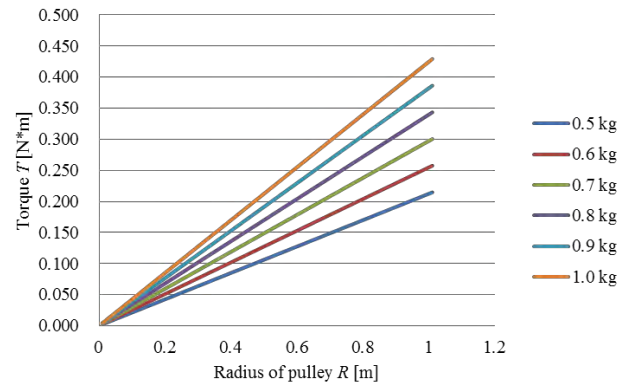


Fig. 5. Estimation of necessary torque performance to compensate the given frictional force

Commercially available torque controllable motor can fit in this range (actually wide range of torque motor is available) so that this design is ensured to work. Currently we are working on constructing the system and be ready to perform the test with gravity sensor.

Remarks

The possibility to eliminate the frictional force is studied and the potential system by generating the constant drag force is proposed. With such devices, introducing the controllable low-gravity device in high accuracy is expected. We will now work to construct the demonstration system to show this concept works properly.

References

- 1) Nakamura, Y. and Sekimoto, K., Transaction of JSASS (special issue for 29th ISTS), in print.

濡れ性が異なる円管を用いた沸騰熱伝達特性に対する重力影響

○大久保 正基, 河南 治 (兵庫県大), Peter STEPHAN, Martin FREYSTEIN,
Felix CRÖßMANN (ダルムシュタット工大)

Influence of Gravity on Heat Transfer of Flow Boiling in Tubes with Different Wettability

○Masaki OKUBO, Osamu KAWANAMI (Univ. Hyogo), Peter STEPHAN, Martin FREYSTEIN,
Felix CRÖßMANN (Tech. Univ. Darmstadt)

1. Introduction

In recent year, exhaust heat, transporting distance of heat and heat generation density of space applications are increasing. In order to solve those problems, flow boiling is a prospective candidate for the cooling system. This system is efficient cooling method because latent heat transfer is caused by phase change under boiling condition. However, heat transfer about flow boiling on μg has many unclear points such as CHF until now. Because of flow boiling is not affected by body force (gravity) in μg , it is expected that boiling bubbles become hard to detach from heating surface and critical heat flux should be decreased. Besides, influences on heat transfer of flow boiling by wettability of heating surface, Phan *et al* reported that heat transfer coefficient at hydrophobic heating surface in rectangular channel (5 mm wide, 0.5 mm height, 180 mm length) increase under the conditions of quality $x = 0.005$ - 0.015 ¹⁾. Here we report that the flow boiling experimental results conducted ESA parabolic flight campaign. Aim of this study is clarify influences of gravity and wettability on flow boiling heat transfer.

2. Experimental Apparatus and Conditions

This boiling flow experiment was conducted under the different gravity levels; μg , 1g and 2g. The test loop is mainly consisted of test section, condenser, tank, pump, flow meter and preheater. The detailed of the test section shown in **Fig. 1** is included three transparent heated tubes (THT) having different wettability of heated surface in series. THT is coated by gold thin film with the thickness of 10-50 nm, it enable to measure

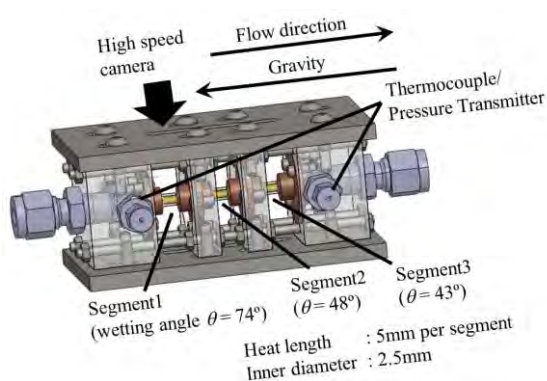


Fig. 1 Test section of parabolic flight experiment

inner wall temperature of the tube, to heat fluid, to observe flow through the wall. The different wettability on the heated wall given by building self-assembled monolayers (SAMs) on the gold film. Tube given SAMs having 1-Dodecanethiol end group as segment1 (wetting angle $\theta = 74^\circ$), normal tube as segment2 ($\theta = 48^\circ$) and tube given SAMs having 11-Mercapto-1-undecanol end group as segment3 ($\theta = 43^\circ$) are located. Flow direction in vertical upward, water is used as a working fluid. Experimental conditions are mass velocity $G = 75$ - $400 \text{ kg/m}^2\text{s}$, subcooling $\Delta T_{sub} = 0.2$ - 11.6 K , loop pressure $P = 0.61$ - 1.16 bar , heat flux $q_{in} = 0$ - 550 kW/m^2 .

3. Results and Discussions

Boiling curve under the conditions of $G = 165 \text{ kg/m}^2\text{s}$, $q_{in} = 0$ - 550 kW/m^2 is shown in **Fig. 2**. Inner wall temperature of the THT at onset nucleate boiling, T_{ONB} , of the segment1 ($\theta = 74^\circ$) is lower than that of segment3 ($\theta = 43^\circ$). In the case of segment1 ($\theta = 74^\circ$), hysteresis of ONB is a little under all of gravity level. On the other hand, segment3 ($\theta = 43^\circ$) has an inference of gravity compared segment1 ($\theta = 74^\circ$). After boiling, influences of gravity did not clear in both tubes under low quality region. The wettability of the heated wall has a small impact in this region; heat transfer of segment3 ($\theta = 43^\circ$) is slightly higher than that of segment1 ($\theta = 74^\circ$).

References

- 1) H. T. Phan, N. Caney, P. Marty, S. Colasson, J. Gavillet: J. Heat Transfer, **134** (2012) 020901-1-6.

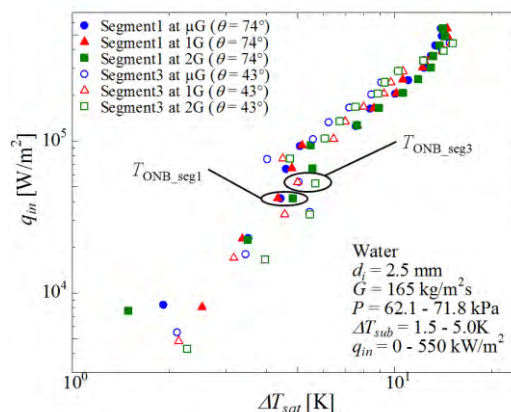


Fig. 2 Boiling curves about segment1 and segment3

沸騰・二相流体ループの加熱円管壁面における気液挙動と熱伝達

○今井智敬, 大久保正基, 河南治 (兵庫県立大), 大田治彦, 新本康久 (九州大), 浅野等 (神戸大), 今井良二 (室蘭工業大), 松本聡, 栗本卓, 高岡秀充, 坂本道人 (JAXA)

Gas-liquid Behavior and Heat Transfer at the Heated Tube Wall in the Boiling and Two-phase Flow Loop

○Tomotaka IMAI, Masaki OKUBO, Osamu KAWANAMI (Univ. of Hyogo), Haruhiko OHTA, Yasuhisa SHINMOTO (Kyushu Univ.), Hitoshi ASANO (Kobe Univ.), Ryoji IMAI (Muroran Institute of Technology), Satoshi MATSUMOTO, Takashi KURIMOTO, Hidemitsu TAKAOKA, Michito SAKAMOTO (JAXA)

1. Introduction

Flow boiling is one of an efficient way to remove large amount of heat. However, there are large amount of research work of pool boiling and flow boiling heat transfer, its physical mechanisms are not yet fully understood. For flow boiling in a tube, Kureta *et al.* reported some “time-averaged” heat transfer data and flow behavior by using short metal heated tube under many experimental conditions¹⁾. However, we could hardly find reports that the relation between transitional heat transfer data and the local gas-liquid behavior on the heated wall of the tube.

In this report, we presents that heat transfer characteristics and flow behavior on the heated wall of the tube by using the short transparent heated tube. A short transparent heated tube which is coated gold thin film on the inner-wall by electroless plating method, it is allowable to measure the averaged inner-wall temperature and to observe flow behavior through the wall at the same time. The tube is installed to understand the mechanism of local heat transfer on flow boiling as an evaporation section, and the relation between transitional gas-liquid behavior and inner-wall temperature will be considered.

2. Results and Discussions

A short transparent heated tube that has 5 mm heated length, 4 mm inner diameter and 6 mm outer diameter as shown in Fig. 1 is used. Fig. 1 is also illustrated the image of flow behavior and its brightness analysis. In this experiment, the focus of camera is tightly focused on the inner-wall of the tube. Fig. 2 is shown an example of the experimental results. The Top figure shows inner-wall temperature of the tube and temporal differentiation of the temperature. Bottom figure shows the ratio of gas-liquid interfacial area to target area. Here, the gas-liquid interface is defined the brightness value below a suitable threshold, 60 which is corresponding green color region in Fig.1. Though the view of camera is only from one direction, it could be found that the transitional tendency of dT/ds and was roughly coincided with the gas-liquid interface ratio. Increasing of the ratio of the gas-liquid interface area caused the decreasing of dT/ds .

References

- 1) M. Kureta, K. Mishima, H. Nishihara, *JSME Ser. B*, **61** (1995), 4109-4116 (in Japanese).

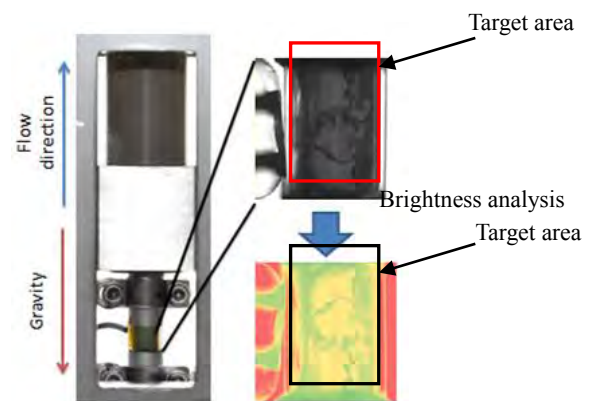


Fig. 1 An enlarged view of short transparent heated tube section (left), an example of flow behavior and its image analysis (right).

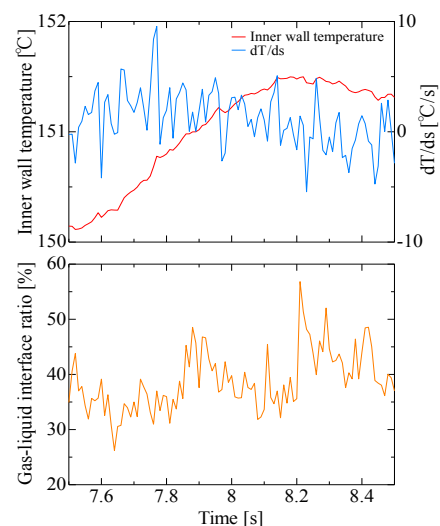


Fig. 2 Histories of inner wall temperature, time changing ratio of temperature (top), the ratio of gas-liquid interface area to target area (bottom) ($G = 47 \text{ kg/m}^2\text{s}$, $q = 395 \text{ kW/m}^2$).

ガスジェット浮遊法とX線散乱を用いた液体 Bi-Ga 合金の構造解析

○北村光汰, 正木匡彦 (芝浦工業大学), 水野章敏 (学習院大学), 小原真司 (SPRING-8)

Structural Analysis of Liquid Bi-Ga Alloy by using X-ray Scattering with Aerodynamic Levitation System

○Kota KITAMURA, Tadahiko MASAKI (Shibaura Institute of Tec), Akitoshi MIZUNO (Gakushuin Univ) and Shinji KOHARA (Spring-8)

1. Introduction

In the gravitational field on the earth, phase separation phenomena in fluids are affected by gravity. Particularly, for the observation of critical phase separation, such as the liquid-liquid or liquid-vapor phase separation, the disturbance by the gravity induces serious problem because the large fluctuation of concentration or density is disturbed by the convective flow. Microgravity environment is regarded as an ideal environment for the research of these kinds. In the previous research, by using sounding rocket, S520, the electrical resistivity of Bi-Ga alloys shows abnormal behavior near the critical point of liquid-liquid phase separation. The behavior might be related to the growth of critical fluctuation, however, the microscopic view of this phenomena is still open question. In addition, it is known that the large concentration fluctuation cause the abnormal behavior of heat capacity, electrical resistivity, and attenuation of sound near the critical point in the homogeneous phase.

In order to grasp an atomic scale phase separation from the liquid phase, neutron or x-ray diffraction experiments is one of the powerful tools. In this study, we tried to observe the structure of liquid Bi-Ga alloy by using the x-ray diffraction combined with the gas levitation and Laser heating.

2. Experiment

Liquid Bi-Ga alloy shows a phase separation with a critical point whose composition is Bi-70atmic%Ga and critical temperature is 535K. The liquid Bi-Ga alloys shows the homogeneous phase at the temperature higher than the critical temperature. The homogeneous liquid alloy is separated into two liquid phases, high density phase and low density phase, at the temperature below the critical temperature.

In this study, the combination of X-ray analysis and jet levitation method was tested to carry out the liquid structure analysis of liquid-liquid phase separation system. We used the two-axis diffractometer of BL04B2 in the SPRING-8. The high-energy X-ray (113.4 keV) was used for the incident x-ray and the angular distribution of scattering intensity was measured due to the Ge detector. The small gas-jet levitation chamber was placed on the diffractometer and the levitated liquid sample was prepared for the diffraction experiments. The sample whose diameter was 2

mm was on the conical nozzle and heated by the focused CO₂ laser which is installed in the experiment hatch. The temperature of sample was measured by using the single color pyrometer. The temperature range of our experiments was 505K~673K. The schematic view of experimental apparatus is shown in Fig. 1.

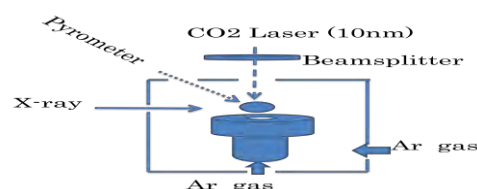


Fig.1 Schematic figure of the gas-jet levitation for the X-ray diffraction experiments

3. Result and Discussion

The structure factor is calculated from scattering intensities obtained from the experiment. The graph in Fig.2 shows structure factor at 535K of Bi-Ga liquid alloys together with that of pure Bi and Ga.

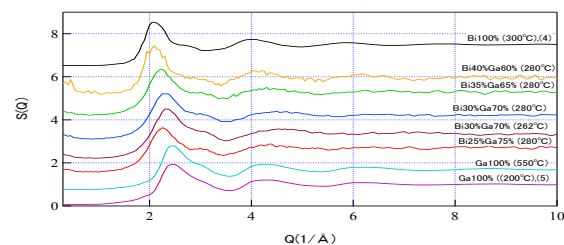


Fig.2 Structure factor of Bi-Ga liquid alloy

A small shoulder was observed in the high wave number side of the first peak of $S(Q)$. The small shoulder is also observed in the structure factor of pure Bi and pure Ga. The features of liquid structure of Bi and Ga were remained even in the liquid mixtures. Positions of first peak of $S(Q)$ shifted to the low Q side when the concentration of Bi was increased.

In the near critical composition, the increase of scattering intensity was observed at the low Q region ($Q < 0.5 \text{ \AA}^{-1}$), which can be regarded as the increase of concentration fluctuation. The relation between the liquid structure and critical phase separation will be discussed in the poster presentation.

微小重力場低圧雰囲気における不等間隔燃料液滴列の燃え広がり特性の実験的調査

○佐野成太, 瀬尾健彦, 三上真人 (山口大)

Experimental Study on Flame-spread Characteristics of Fuel Droplet Arrays with Uneven Droplet Spacing at Low Pressure in Microgravity

○Narita SANO, Takehiko SEO, Masato MIKAMI (Yamaguchi Univ.)

1. Introduction

Spray combustion is widely used in gas turbine engines and diesel engines. In order to elucidate basic flame spread mechanisms, many researchers have investigated flame spread of droplet arrays at normal pressure¹⁾⁻³⁾ and high pressures⁴⁾ in microgravity. The droplet diameter is several μm order in spray combustion, which is not affected by the natural convection. In the experiment, it is necessary to use the droplet diameter of 1 mm order for observation with high resolution. In this case, however, the effect of the natural convection cannot be ignored in normal gravity. Therefore, experiments have been carried out in micro-gravity to ignore the effects of natural convection.

The fuel droplets distribute randomly in spray combustion. Droplet spacing affects the characteristics of flame-spread. Mikami et al.²⁾ experimentally investigated the flame-spread limit distance between droplets at normal pressure in microgravity. Oyagi et al.³⁾ conducted flame-spread experiment in microgravity using droplet arrays with uneven droplet spacing and reported that the flame-spread limit distance increases by two-droplet interactive combustion. The flame-spread experiments of an n-decane droplet array were conducted in microgravity at pressures up to 5.0 MPa by Kobayashi et al.⁴⁾. The effects of ambient pressure on flame spread phenomena were investigated. However, the flame spread phenomena at low pressures have not been reported. This research experimentally investigated flame-spread limit distance and flame-spread rate of fuel-droplet array with uneven droplet spacing in microgravity at low pressure.

2. Experimental apparatus and method

Figure 1 shows the experimental apparatus. It consists of the droplet generation system, the two-dimensional traverse system, the ignition system and the low pressure vessel. The droplets are placed at SiC fiber intersections¹⁾. The diameter of SiC fiber is 14 μm . The liquid fuel, n-decane, is supplied to intersections of SiC fibers through a glass needle. The glass needle is connected to a motor-driven micro-syringe through Teflon tube to supply the fuel. The generated droplet diameter was 0.5 mm. Figure 2 shows the definition of the droplet array with uneven droplet spacing. Droplet I is the droplet for ignition. Droplets A and B are interactive droplets. Droplet L is the droplet to investigate the flame-spread characteristics. The Droplet I was ignited by a hot-wire igniter made of Fe-Cr. The droplet spacing between

Droplets I and B was $S_{IB}/d_0 = 18$ so that heat from the igniter does not affect to other droplets than Droplet I and the interaction between burning Droplets I and B is negligible. The initial droplet diameter d_0 was estimated as 0.48 mm at the ignition timing. Flame-spread behavior was recorded by a digital video camera. The framing rate of the camera was 240 fps. The low pressure atmosphere field was formed by removing air from inside of the vessel by a vacuum pump. All the experiments were conducted at 25 kPa in microgravity. Microgravity conditions were attained by dropping the apparatus with a drag shield in the drop facility at the Yamaguchi University, which provides about 0.95 s microgravity conditions.

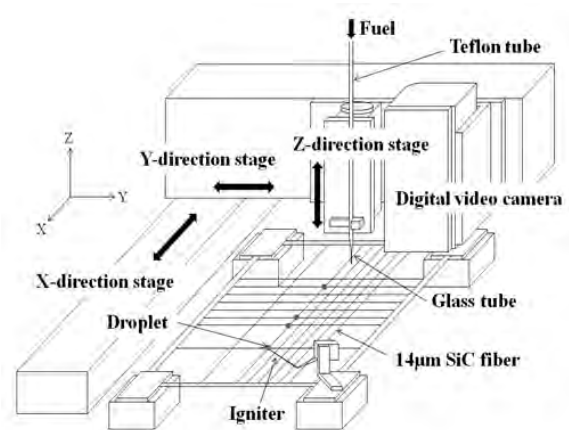


Fig. 1 Experimental apparatus

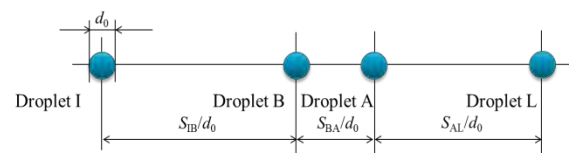


Fig. 2 Droplet-array model

3. Results and discussion

Figure 3 shows direct images of flame-spread behavior of fuel-droplet array for $S_{BA}/d_0 = 4.2$ and $S_{AL}/d_0 = 27.1$ at 25 kPa. Figure 4 shows direct images of flame-spread behavior for $S_{BA}/d_0 = 4$ and $S_{AL}/d_0 = 16$ at 101 kPa. These values of S_{AL}/d_0 are near the flame-spread limit distance for each pressure. In Fig. 3, blue flame was always observed through combustion at 25 kPa.

This indicates the soot formation was suppressed. However, at 101 kPa, yellow luminosity from emission of soot was observed. Elapsed time t/d_0^2 is from the ignition of Droplet A. The initial flame around Droplet L was observed at $t/d_0^2 = 1.83 \text{ s/mm}^2$ and flame-spread rate was calculated as $V_f d_0 = 25.0 \text{ mm}^2/\text{s}$ at 25 kPa. On the other hand, the initial flame around Droplet L was observed at $t/d_0^2 = 0.88 \text{ s/mm}^2$ and flame-spread rate was calculated as $V_f d_0 = 21.6 \text{ mm}^2/\text{s}$ at 101 kPa. The flame-spread rate at 25 kPa is faster than at 101 kPa although the flame-spread limit distance at 25 kPa is larger than that at 101 kPa.

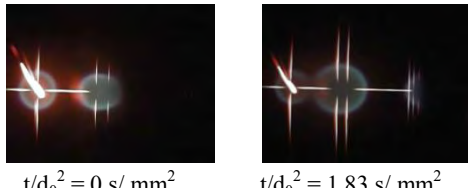


Fig. 3 Flame-spread behavior at 25 kPa

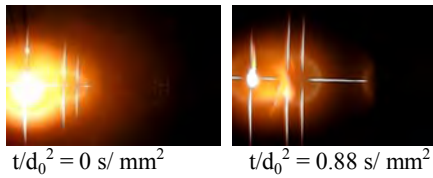


Fig. 4 Flame-spread behavior at 101 kPa

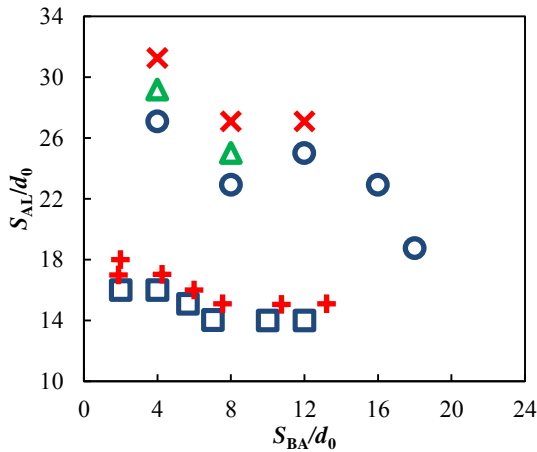


Fig. 5 Dependences of local flame-spread limit distance on the droplet spacing S_{BA}/d_0 for interactive two droplets. The data in the lower half part are for 101 kPa³⁾ and the data in the upper half part are for 25 kPa.

Figure 5 shows the local flame-spread-limit distance of droplet array with two-droplet interaction between Droplets B

and A. \circ symbol represents the droplet spacing S_{AL}/d_0 if the flame-spread occurred, \triangle symbol represents S_{AL}/d_0 if the probability of flame-spread occurrence was from 25% to 75%, and \times symbol represents S_{AL}/d_0 if the flame spread did not occur at 25 kPa. \square symbol represents the droplet spacing S_{AL}/d_0 if the flame-spread occurred, $+$ symbol represents S_{AL}/d_0 if the flame spread did not occur at 101 kPa reported by Oyagi et al³⁾. The flame-spread-limit distance $(S_{AL}/d_0)_{\text{limit}}$ exists between \circ and \times . Those results show the flame-spread-limit distance at 25 kPa is greater than that at 101 kPa.

Figure 6 shows the relationship between flame-spread distance and flame-spread rate. \diamond symbol shows the flame-spread rate without interactive effect calculated from flame-spread time and droplet spacing between Droplet B and A. \triangle symbol shows the flame-spread rate in interactive condition of $S_{BA}/d_0 = 4.2$. Considering the fact that the flame-spread rate decreases with increasing the flame-spread distance²⁾, Fig. 6 suggests that the flame-spread rate increases with interactive effect of two droplets at 25 kPa.

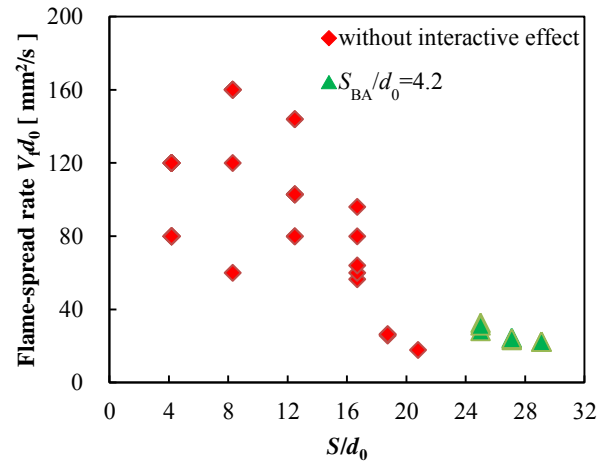


Fig. 6 Relationship between flame-spread distance and flame-spread rate

4. Conclusions

This research experimentally investigated flame-spread-limit distance and flame-spread rate of fuel-droplet-array with uneven droplet spacing in microgravity at low pressure.

- (1) The flame-spread-limit distance at 25 kPa is greater than that at 101 kPa.
- (2) The flame spread rate increases with interactive effect of two droplets at 25 kPa.

Acknowledgments

This research was partly subsidized by Grant-in-Aid for Scientific Research (B) (24360350). We wish to thank Mr. N. Motomatsu for his valuable help in experiments.

References

- 1) M. Mikami, H. Oyagi, N. Kojima, M. Kikuchi, Y. Wakashima, S. Yoda, "Microgravity experiments on flame spread along fuel-droplet arrays using a new droplet-generation technique", *Combustion and Flame*, **141**,(2005), 241-252.
- 2) M. Mikami, H. Oyagi, N. Kojima, M. Kikuchi, Y. Wakashima, S. Yoda, "Microgravity experiments on flame spread along fuel-droplet arrays at high temperatures", *Combustion and Flame*, **146**,(2006),391-406.
- 3) H. Oyagi, H. Shigeno, M. Mikami, N. Kojima, "Flame-spread probability and local interactive effects in randomly arranged fuel-droplet arrays in microgravity", *Combustion and Flame*, **156**,(2009),763-770.
- 4) H.Kobayashi, J Park, T Iwahashi, T Nioka, "Microgravity experiments on flame spread of n-decane droplet array in a high-pressure environment", *Proceedings of the Combustion Institute*, **29**, (2002), 2603-2610.

雰囲気酸素分圧依存性を考慮した銅および銀融体の無容器表面張力測定

○西村大, 武井悠翔, 工藤優, 小澤俊平 (千葉工大)

Containerless Measurement of Surface Tension of Molten Copper and Silver in Consideration of Oxygen Partial Pressure of Atmospheric Gas

○Masaru NISHIMURA, Yuto TAKEI, Yu KUDO, Shumpei OZAWA (Chiba Inst. Tech.)

1. Introduction

Surface tension of high temperature molten metals is one of the most important thermophysical properties to improve and optimize various high temperature melt processes involving a free surface such as welding and blazing, because surface tension difference is a driving force of the Marangoni convection.

It is known that oxygen acts as strong surfactant for molten metals. Because oxygen can exist as gas phase even at room temperature, surface tension of molten metals is influenced by oxygen partial pressure of measurement atmosphere, P_{O_2} ^{1),2)}. However little attention has been given to the influence of P_{O_2} on surface tension of molten metals. A conventional container technique of the surface tension measurement such as the sessile drop method can only assure the measurement at a comparatively low temperature in order to prevent a chemical reaction between the sample and the measurement device.

In this study, surface tension of molten copper and silver was measured by oscillating droplet method using electromagnetic levitation (EML) free from container. P_{O_2} of the atmospheric gas was controlled by gas phase equilibrium using H_2 - H_2O mixtures. The purpose of this study was to measure an accurate surface tension of molten copper in consideration of influence of P_{O_2} .

2. Experimental procedure

High purity cubical copper was electromagnetically levitated and then melted under flow condition of the Ar-He- H_2 - H_2O mixed gas. The P_{O_2} of the inlet gas was confirmed by zirconia oxygen sensor operated at 1008 [K]. The sample temperature was controlled by flow ratio of argon and helium gases. The surface tension of the sample was calculated from the droplet oscillations using the Rayleigh equation³⁾ calibrated by Cummings and Blackburn⁴⁾. The details of the experimental procedure is shown elsewhere²⁾.

3. Results

Figure 1 shows the surface tension of molten copper measured by oscillating droplet method using EML. We successfully measured surface tension of molten copper over a very wide temperature of about 500K under well controlled P_{O_2} conditions. When the P_{O_2} is less than 10^{-8} Pa below 1840 K

under the Ar-He-10vol.% H_2 gas atmosphere, the surface tension is decreased with increasing temperature. When the P_{O_2} is precisely controlled at 10^{-8} , 10^{-7} and 10^{-6} Pa under the gas equilibrium using Ar-He- H_2 - H_2O mixtures, the boomerang shape temperature dependence of surface tension for molten copper is observed: the surface tension increases once and then decreases with rising the temperature as in the case of molten iron and nickel^{2),5)}. This boomerang shape temperature dependence of surface tension can be explained by the temperature reliance of equilibrium constant for oxygen adsorption reaction. Higher P_{O_2} usually induces lower surface tension due to oxygen adsorption at comparatively low temperature. However oxygen is desorbed from the melt surface with increasing temperature because the equilibrium constant of oxygen adsorption reaction decreases as the sample temperature rises. In this case, the surface tension approaches to the pure state value. Consequently, the surface tension becomes almost the same as the surface tension of pure state at high temperature.

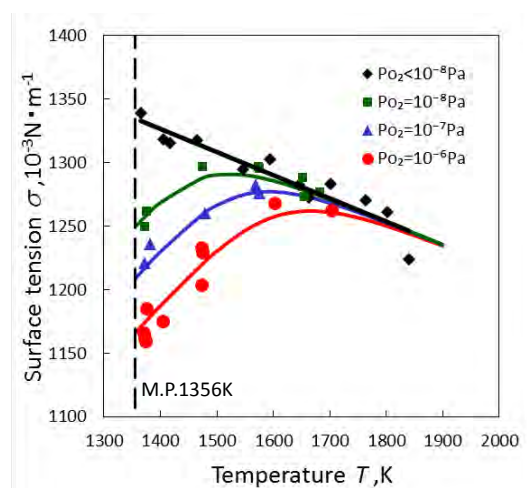


Fig. 1 Surface tension of molten copper

References

- 1) K. Mukai, Z. Yuan, K. Nogi, T. Hibiya: ISIJ Inter., **40**, (2000)148.
- 2) S. Ozawa, S. Suzuki, T. Hibiya, and H. Fukuyama: J. Appl. Phys., **109**,(2010), 014902.
- 3) Lord Rayleigh: Proceeding of The Royal Society of London **29**,(1879)71
- 4) D. L. Cummings, D. A. Blackburn: J. Fluid Mech. **224**, (1991)395.
- 5) S. Ozawa, S. Takahashi, and Y. Takei: IJST2013 abstract.

微小重力場における二液滴の冷炎・熱炎発生位置の観測

○米康太, 岩本武尊, 橋本英樹, 森上修, 村瀬英一 (九州大)
野村浩司 (日本大), 菊池政雄 (宇宙航空研究開発機構)

Observation of Locations of Cool-Flame and Hot-Flame Appearances around a Fuel Droplet Pair in Microgravity

○Kota YONE, Takeru IWAMOTO, Hideki HASHIMOTO, Osamu MORIUE, Eiiichi MURASE (Kyushu Univ.), Hiroshi NOMURA (Nihon Univ.), Masao KIKUCHI (JAXA)

1. Introduction

It is well known from the studies on homogeneous gas mixtures that two-stage ignition occurs for most hydrocarbon fuels. In two-stage ignition, cool flame, which is induced by the low-temperature oxidation reactions and has almost no light emission, appears first, and then hot flame, which is induced by the high-temperature oxidation reactions, appears. The two-stage ignition has been experimentally observed even for spontaneous ignition of *n*-alkane droplets¹⁾, which indicated that spontaneous ignition of a fuel spray must be analyzed with attention to two-stage ignition behavior. Spontaneous ignition of a fuel droplet in hot air has been studied by many researchers as a fundamental study for fuel-spray ignition. An isolated droplet is physically the simplest model of a fuel spray. If the effect of buoyancy is negligible, the phenomenon is spherically symmetric, which simplifies the comparison between experiments and theoretical or numerical analysis. However, there exists interaction between droplets in a fuel spray, and its effect cannot be taken into account by an isolated droplet. Droplet interaction is supposed to have two counteracting effects. One is mutual cooling effect between droplets through multiplied heat sinks, and the other is enhanced fuel supply through multiplied fuel sources. In order to investigate the effect of the droplet interaction, spontaneous ignition of a fuel droplet pair was experimentally studied by the authors' group in μg ²⁾. As seen in Fig. 1, the results showed that smaller inter-droplet distance, l , led to longer cool-flame ignition delay, τ_{cf} , and shorter second induction time, τ_2 , the duration between cool-flame appearance and hot-flame appearance. The results implied that the mutual cooling effect was dominant before cool-flame appearance, while the effect of duplicated fuel sources was dominant after cool-flame appearance. Such tendency is caused by the development of non-spherical distributions of temperature and fuel concentration, and is supposed to be related with the locations of cool-flame and hot-flame appearances. In order to observe those locations, two-dimensional observation was attempted with Michelson interferometer, which enables the detection of cool flame³⁾, and one data was obtained in μg . In this study, the locations of cool-flame and hot-flame appearances were further sought in μg , and the effect of l and ambient temperature, T_a , was examined.

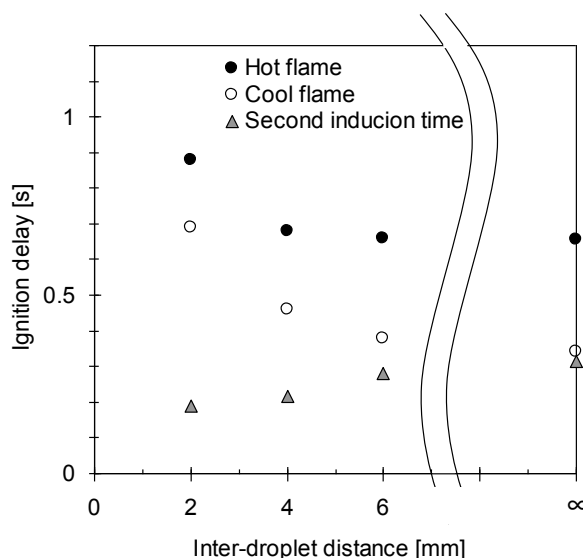


Fig. 1 Effects of inter-droplet distance on cool-flame and hot-flame ignition delays and second induction time (*n*-decane, 1 mm droplet, 0.3 MPa, 650 K, μg)²⁾

2. Experimental Apparatus and Procedure

The experimental apparatus is composed of a high-pressure chamber, optical recording system and controlling system. The high-pressure chamber contains an electric furnace, a droplet-pair suspender, a suspender driving device and a fuel supplying device. The inner volume of the furnace is 41 mm in diameter and 40 mm in height. The temperature inside the furnace was controlled to be a desired value. The fuel droplets were generated on the intersections of 14 μm SiC fibers at room temperature. The distance between the two droplet centers was defined as l , and was 2 mm or 4 mm. Fuel was *n*-decane, and its normal boiling point is 447 K. Initial droplet diameter, d_0 , was 1 ± 0.05 mm. The droplet pair was inserted into the furnace, which was located over the pair, and thus exposed from room temperature to high temperature rapidly. The transition time from room temperature to high temperature was about 50 ms. He-Ne laser (wave length: 633 nm, power: 0.84 mW) was used as a light source of Michelson interferometer. The laser beam was expanded to 20 mm in diameter and led into the furnace through the windows. The direction of the laser beam was

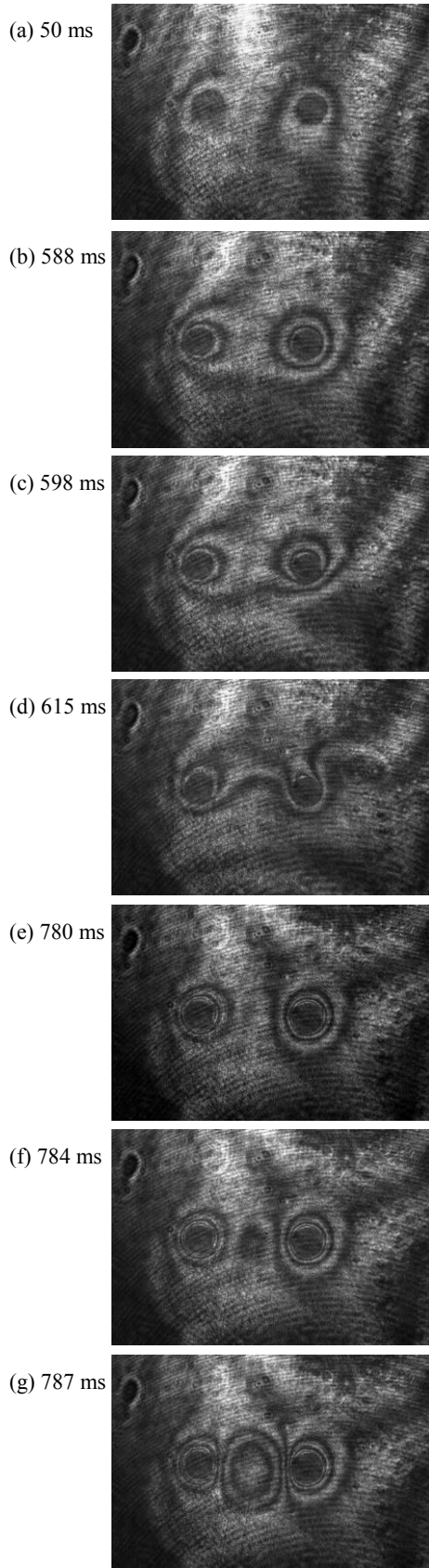


Fig. 2 Images of spontaneously igniting droplet pair through interferometry ($P=0.3$ MPa, $T_a=620$ K, $l=4$ mm, fuel: *n*-decane, $d_0=1$ mm, μg , 1000 fps)

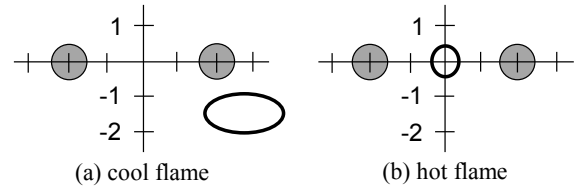


Fig. 3 Locations of cool-flame and hot-flame appearances ($P=0.3$ MPa, $T_a=620$ K, $l=4$ mm, fuel: *n*-decane, $d_0=1$ mm, μg)

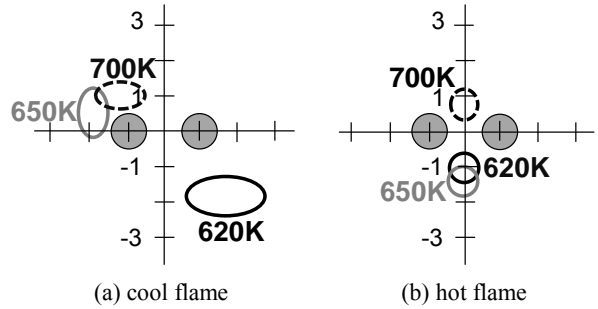


Fig. 4 Locations of cool-flame and hot-flame appearances for different T_a ($P=0.3$ MPa, $l=2$ mm, fuel: *n*-decane, $d_0=1$ mm, μg) Temperatures in the figures indicate T_a .

perpendicular to the plane containing two droplets. Thus, density distribution in the furnace was able to be qualitatively observed as fringes. The images were recorded by a high-speed camera with a frequency of 1000 fps. Ambient pressure, P , was 0.3 MPa, and T_a was between 620 and 700 K. The drop tower “COSMOTORRE” (μg duration: 2.5 s) of HASTIC (Hokkaido Aerospace Science and Technology Incubation Center) was used as microgravity facility.

3. Results and Discussion

Figure 2 shows the images abstracted from the movie for $T_a=620$ K and $l=4$ mm. The droplet pair ended its travel into the furnace at Fig. 2 (a) 50 ms. Then fuel vapor layer developed around the droplet pair quasi-steadily until Fig. 2 (b) 588 ms. Almost axial symmetric fringes show that temperature distribution was also almost axial symmetric. There was a change in fringes at right down side of the right droplet in Fig. 2 (c) 598 ms, which shows that there was a heat release by cool flame. The fringes shifted towards two droplets (Fig. 2 (d) 615 ms), which shows that cool flame was going to surround the droplet pair. Then quasi-steady state lasted again until Fig. 2 (e) 780 ms. In Fig. 2 (f) 784 ms and (g) 787 ms, sudden and narrow change in fringes was observed in the middle point of two droplets, which shows that there was a heat release by hot flame. The locations of cool-flame and hot-flame appearances obtained from Fig. 2 are shown in Fig. 3. Two circles filled with gray color show two droplets, and unfilled ellipse or circle shows the location of cool-flame or hot-flame appearance. Scale of the coordinate is in mm. Location of cool-flame

appearance is not as apparent as that of hot flame, and therefore its location is wider. Such measurements were performed for several T_a at $l=2\text{mm}$, and the locations of cool-flame and hot-flame appearances are shown in Fig. 4. Temperatures near ellipses or circles show T_a . For all T_a , cool flame appeared on the outer side of the droplet pair, and hot flame appeared on the plane located in the middle of two droplets. The previous study ²⁾ implied that temperature is dominant for cool-flame appearance. The present results correspond with the previous study, since the temperature on the outer side of the droplet pair is higher. The previous study ²⁾ also implied that fuel concentration is dominant for hot-flame appearance. The present results also correspond with the previous study, since the fuel concentration on the inner side of the droplet pair is higher than that on the outer side.

4. Conclusions

In order to study the droplet interaction in spontaneous ignition of a fuel spray, spontaneous ignition of a fuel droplet pair was observed with interferometer in μg . Cool flame appeared on the outer side of the droplet pair, and hot flame appeared on the inner side of the droplet pair. The results correspond with the discussion in the previous study on the development of non-spherical distributions of temperature and fuel concentration. Further examination for wider experimental conditions are expected.

References

- 1) O. Moriue and M. Tanabe: Atomization (Journal of the ILASS-Japan), **17**, 57 (2008) 22. (in Japanese)
- 2) O. Moriue, Y. Nishiyama, Y. Yamaguchi, H. Hashimoto and E. Murase: Proc. Combust. Inst., **34** (2013) 1585.
- 3) O. Moriue, R. Takagi, K. Yone, H. Hashimoto, E. Murase, K. Kaneko, H. Nomura and M. Kikuchi: Trans. JSASS Aerospace Tech. Japan, **12**, ists29 (2014) pp. Ph_13.

荷電コロイドの電荷誘起結晶化と結晶構造

○柿原千穂, 豊玉彰子, 奥菌透, 山中淳平 (名古屋市立大学),
篠原忠臣, 谷川正幸, 曾我見郁夫 (京都産業大学)

Charge-Induced Crystallization and Crystal Structures of Ionic Colloids

○ Chiho KAKIHARA, Akiko TOYOTAMA, Tohru OKUZONO, Junpei YAMANAKA (Nagoya City Univ.),
Tadatomi SHINOHARA, Masayuki TANIGAWA, Ikuo SOGAMI (Kyoto Sangyo Univ.)

1. Introduction

Submicron-sized charged colloidal particles dispersed in liquid medium self-assemble into ordered “crystal” structures, where the particles are regularly arranged in the body-centered-cubic (bcc) or face-centered-cubic (fcc) lattices. We have been studying the charge-induced crystallization of dilute charged colloids (1-4) in the Space Experiment Project on Colloidal Crystallization (Director: Professor Emeritus Ikuo Sogami, Kyoto Sangyo University). In the present paper we report the bcc/fcc structural phase transition of the charged colloids upon increasing the particle concentration and varying the charge number.

2. Materials and Methods

Polystyrene (PS) spheres were prepared by using an emulsion-free radical polymerization method. The reaction solution (water/methanol mixtures) containing styrene (monomer), sodium *p*-styrenesulfonate (charged monomer), divinylbenzene (cross-linker), and potassium persulfate (polymerization initiator) were stirred at 80 °C under a nitrogen atmosphere. Three kinds of particles, KSS-5 (the diameter $d = 118$ nm; charge number $Z = 1245$), KSS-6 ($d = 109$ nm; $Z = 1233$), and KSS-8 ($d = 117$ nm; $Z = 1911$) were synthesized.

Reflection spectrum of the crystals were measured by using fiber optics spectrophotometers USB2000 and NIR-512, Ocean Optics Co., Ltd. Laser diffraction measurements were performed by means of Kossel diffraction apparatus constructed in Kyoto Sangyo University.

3. Results and Discussion

Figure 1 (a) and 1(b) show the diffraction wavelength λ of the KSS-5 and 6 samples. The symbols are observed values (filled square, open square, and open circles show the first, second, and third diffractions, respectively). The solid and dot-dashed curves represent calculated values for fcc and bcc lattices. It is clearly seen that the crystal exhibited the phase transition from bcc to fcc lattice structure on increasing the particle concentration for both the samples.

We observed that the colloid having higher surface Z

showed the bcc to fcc transition at the lower particle concentrations. Comparisons between the Kossel diffraction measurements and reflection spectrum will be presented.

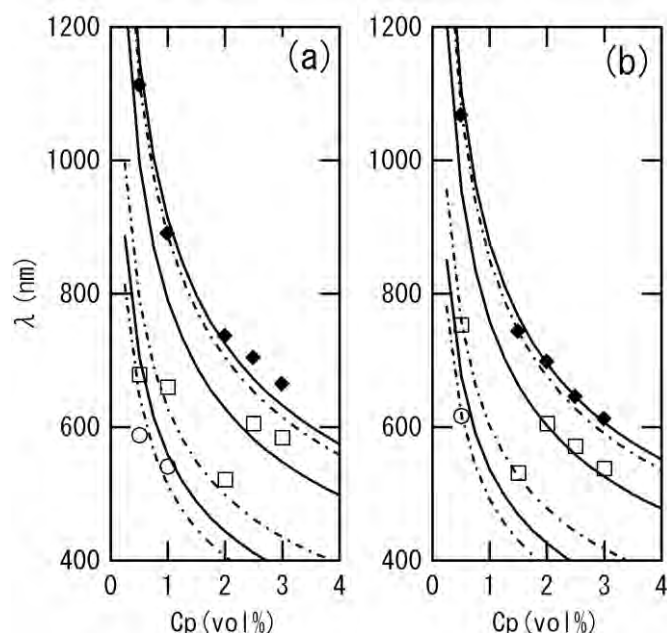


Fig.1 Variations of diffraction wavelengths from colloidal crystals upon changing the particle concentration determined by using reflection spectrum (a) KSS-5 and (b) KSS-6. Symbols, observed wavelengths; curves, calculated values for bcc (dash-dotted) and fcc (solid) crystals.

References

- 1) J.Yamanaka, T.Koga, N.Ise, and T.Hashimoto, Phys.Rev. E 53(1996) R4317.
- 2) J.Yamanaka, H.Yoshida, T.Koga, N.Ise, and T.Hashimoto, Phys. Rev. Lett., 80(1998) 5806.
- 3) H.Yoshida, J.Yamanaka, Ta.Koga, Ts.Koga, N.Ise, and T.Hashimoto, Langmuir, 15(1999)2684.
- 4) A.Toyotama, T.Sawada, J.Yamanaka, K.Kitamura, Langmuir, 19(2003) 3236.

燃焼限界統一理論の構築に向けた微小重力場における極低速予混合対向流実験

○小林友哉, 中村寿, 高瀬光一, 手塚卓也, 長谷川進 (東北大), 丸田薫 (東北大, 極東連邦大), Roman FURSENKO, Sergey MINAEV (極東連邦大), 勝田真登, 菊池政雄 (JAXA)

Low-speed Premixed Counterflow Experiments under Microgravity for a Comprehensive Combustion Limit Theory

○Tomoya KOBAYASHI, Hisashi NAKAMURA, Koichi TAKASE, Takuya TEZUKA, Susumu HASEGAWA (Tohoku Univ.), Kaoru MARUTA (Tohoku Univ., Far Eastern Federal Univ.), Roman FURSENKO, Sergey MINAEV (Far Eastern Federal Univ.), Masato KATSUTA, Masao KIKUCHI (JAXA)

1. Introduction

Due to recent demand for higher efficiency combustors, the oxy-fuel combustion is drawing attention. The oxy-fuel combustion uses fuel, pure oxygen, and recirculated CO₂ in burned gas. To develop such combustors, an accurate and a comprehensive understanding of combustion limits with high concentrations of CO₂ is needed. In past studies, combustion limits of flames have been investigated based on the counterflow method under μg to rule out the effect of natural convection¹⁾. However, parallel studies to this have revealed the existence of non-propagating spherical flames, flame balls, beyond the limit of planar propagating flames²⁾. Since both of these flames have been investigated separately, there are only limited attempts to bridge the limits of these two flames. For discussion on absolute combustion limits, a theory that encompasses both of these flames is required.

A recent study utilizing the counterflow method under μg for extremely low stretch rates with CH₄/O₂/Xe mixtures have succeeded in obtaining a transition from planar flames to ball-like flames³⁾. However, the effect of radiation on the transition and on combustion limits has not been investigated. Therefore, the goal of this research is to provide a benchmark data connecting counterflow flames and flame balls, and to provide an understanding on the effects of radiation on the combustion limits for the development of oxy-fuel combustors.

2. Experimental Method

Counterflow experiments under microgravity were conducted on the airplane MU-300 provided by the Diamond Air Service Inc. Two opposing burners with an inner diameter of 3.0 cm and separation distance of 3.0 cm were used inside a chamber to obtain the counterflow field. To observe the flame, a high-speed camera equipped with an image intensifier was used. The employed mixture is CH₄/O₂/CO₂ where the ratio of O₂ to CO₂ mole fraction is 0.4. Previous studies with Xe diluted mixtures for the same setup have been conducted to obtain low-Lewis numbers, showing that if the stretch rate is low enough, a transition from planar flames to ball-like flames will occur³⁾. Here, a Lewis number is the ratio of the diffusion and the heat diffusion coefficients.

3. Results

Figure 1 shows the flame obtained in the microgravity experiments for CO₂ diluted mixtures at the mixture velocity of 4.8 cm/s (stretch rate = 3.2 s⁻¹) at the burner outlet. Initially, the flames are twin planar flames. Then, as the equivalence ratio is decreased, the flame forms a single planar flame. Finally, a transition to a ball-like flame was observed before extinction. This indicates that, similarly to Xe diluted mixtures, transition from planar propagating flames to ball-like flames and then to flame balls may occur. For CO₂ diluted mixtures, ball-like flames were observed from equivalence ratio 0.49 to 0.48, whereas for Xe diluted mixtures, ball-like flames were observed from equivalence ratio 0.37 to 0.35. It can be observed that the equivalence ratio range is both narrow and at a higher region for CO₂ mixtures than Xe for diluted mixtures. This is a result of the difference in Lewis number and the amount of radiative heat loss.

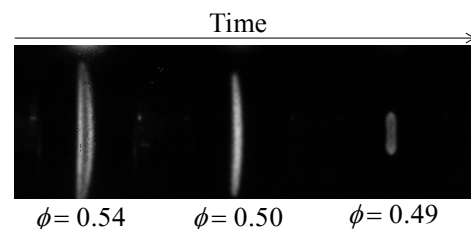


Fig. 1 Images of experimental counterflow flames at 4.8 cm/s.

4. References

- 1) K. Maruta, M. Yoshida, Y. Ju and T. Niioka: Proc. Combust. Inst., **26** (1996) 1283.
- 2) P. D. Ronney, M. S. Wu, H. G. Pearlman, K. J. Weiland: AIAA Journal, **36** (1998) 1361.
- 3) K. Takase, X. Li, J. Nakamura, T. Tezuka, S. Hasegawa, M. Katsuta, M. Kikuchi, K. Maruta: Combust. Flame, **160** (2013) 1235.

5. Acknowledgements

A part of this study was supported by JAXA and JSF by the latter half of the second utilization phase of the KIBO pressurized module project. Also, a part of this study was supported financially by the Ministry of education and science of Russian Federation (project 14.Y26.31.0003).

熔融塩中での月土壌シミュラントからの金属採取

○坂中佳秀, 後藤琢也 (同志社大), 石川毅彦, 高柳昌弘 (JAXA), 福中康博 (JST)

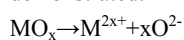
Extraction of Metal in Molten Salt from Lunar Regolith Simulant

○Yoshihide SAKANAKA, Takuya GOTO (Doshisha Univ.), Takehiko ISHIKAWA, Masahiro TAKAYANAGI (JAXA), Yasuhiro FUKUNAKA (JST-CREST)

1. Introduction

Considering the construction of lunar base, the high cost of transporting materials from Earth to the Moon is important problem. Therefore, in situ resource utilization is a key component of space exploration. Because of the high cost of transporting material from Earth to the Moon, we need to use lunar resource to make all components. If silicon and other metals could be produced on the moon, it would provide some advantages.

Lunar crust is known to be rich in mineral resources, for example, lunar regolith contains metallic elements such as silicon, titanium, aluminum and so on. For using the mineral resources, development for extracting process of the minerals is essential. From the background, electrochemical extraction of silicon and other metal in molten salts dissolved silica or lunar regolith simulant has been proposed and experimentally demonstrated.



In this presentation, the electrochemical behavior of SiO_2 and lunar regolith simulant in molten salt and property of obtained samples will be presented.

2. Experimental

All experiments were performed in LiF-NaF-KF or LiF-KF-BaF₂ eutectic melts in dry argon atmosphere. The cell was alumina crucible in a cylindrical vessel made of refractory steel and closed by a stainless steel lid. The cell was heated using a programmable furnace and temperature was measured using a chromel-alumel thermocouple.

SiO_2 or lunar regolith simulant were added directly to the melts as silicon or metal ion source respectively. For the investigation of electrochemical behavior, Ag and Ni wire were used as working electrode. A potentiostat/galvanostat (Hokuto Denko Co. Ltd. HZ-3000) was used for electrochemical measurements.

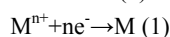
The samples were prepared by potentiostatic electrolysis and rinsed with AlCl_3 solution. The obtained samples were characterized by X-ray diffraction. Morphologies of samples were observed by scanning electron microscope.

3. Results

In order to investigate the electrochemical behavior of lunar regolith simulant, cyclic voltammetry was conducted in a molten LiF-KF-BaF₂ at 873 K.

Fig. 1 shows the cyclic voltammograms for Ni electrode before and after addition of lunar regolith simulant. The dotted curve presents the before and the solid curve presents the after addition of lunar regolith simulant.

After addition of lunar regolith simulant, on the cathodic sweep, a cathodic current was observed at approximately 1.0 V. This cathodic current is attributed to metal deposition as shown in reaction (1)



Based on the results of cyclic voltammetry, Ni plate was used as the cathode and potentiostatic electrolysis was carried out at 0.2 V for 1 h in LiF-KF-BaF₂ containing lunar regolith simulant at 873 K.

From the result of XRD analysis of the sample, the observed peaks were identified as Ni, originating from the substrate, Si and Ni₃₁Si₁₂. Further analysis was conducted to investigate the elements of the sample. From the EDS analysis, obtained sample containing Si, Ti and Al.

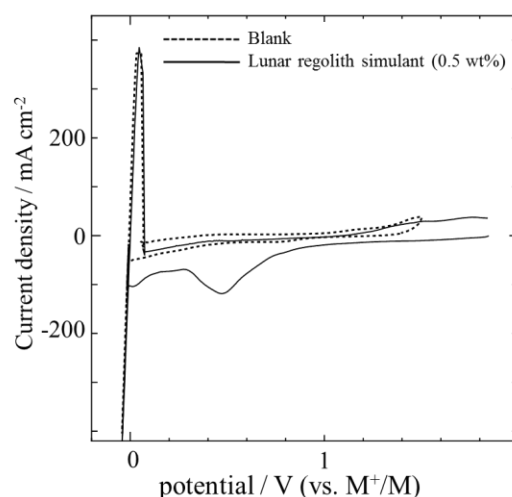


Fig. 1. Cyclic voltammograms for a Ni electrode in LiF-KF-BaF₂ eutectic before and after addition of 0.5 wt% lunar regolith simulant at 873 K. Scanning rate: 0.1 V s⁻¹.